JM PAPERS

# Supply mechanisms of the geostrophic mode in rotating turbulence: interactions with self, waves and eddies

H. Lam[1],†, A. Delache[1,2] and F.S. Godeferd[1]

[1]Université de Lyon, École centrale de Lyon, CNRS, Université Claude Bernard Lyon 1, INSA Lyon, LMFA, UMR5509, 69130 Ecully, France

[2]Université Jean Monnet, 42100 Saint-Étienne, France

Direct numerical simulations are performed in rotating turbulence for different regimes at various Rossby and inertial Reynolds numbers ($Re_I$). A new algorithm, adapted from stratified turbulence (Lam *et al.*, *J. Fluid Mech.*, vol. 923, 2021, A31) to rotating turbulence, permits to separate the three-dimensional velocity field into three parts: inertial waves (IWs), eddies and a geostrophic mode (GM). It uses the space–time properties of waves and their advection by the GM to filter the IWs from the rest of the motion. We obtain balance equations for the separate energies of waves, eddies and the GM. Their mutual interactions are evaluated and analysed via Sankey diagrams that provide a global picture of energy exchanges. When the flow is forced at large scale, it mainly feeds the wave part and the multiple interactions lead to energy dissipation in eddy and GM motion. We also show that, in addition to the wave/wave interaction that feeds the GM, corresponding to different mechanisms described in the literature, other non-documented interactions feed it, as the eddy/wave interaction or the eddy/eddy interaction at moderate $Re_I$. We propose a scale-by-scale analysis of the transfer to the GM: we show that transfers from wave or eddy occur at large scale, that they either inject or remove energy, and that this occurs with or without direct cascade depending on the kind of interaction, wave/wave, eddy/wave or eddy/eddy. The self-interaction of the GM is an inverse cascade for its horizontal component, shaping it into a very large-scale flow.

**Key words:** rotating turbulence, wave-turbulence interactions, waves in rotating fluids

## 1. Introduction

Rotating turbulence is encountered in geophysical contexts such as in the atmosphere or the ocean, but also in industrial flows in turbomachines for energy production or propulsion.

† Email address for correspondence: henri.lam@ec-lyon.fr

A rotating flow can result in different kinds of motions, such as propagating inertial waves (IWs), rotating eddies and what is commonly called a geostrophic mode noted GM (also called slow mode or slow manifold in the literature, though the terminology of GM was introduced by Greenspan 1969), which are entangled and interact together (Godeferd & Moisy 2015). Inertial waves have been detected and characterized in rotating turbulence experiments (e.g. Yarom & Sharon 2014; Campagne *et al.* 2015) and numerical simulations (e.g. Di Leoni, Cobelli & Mininni 2015; Le Reun *et al.* 2017). Most studies show that, compared with IWs or eddies, the GM is often a powerful large-scale vortex invariant along the rotational axis, evolving slowly in time and characterized by an equilibrium between the Coriolis force and horizontal pressure gradients (e.g. Godeferd & Moisy 2015; Sagaut & Cambon 2018). Such a large-scale structure has been observed in a wide variety of rotating flow experiments as in Brunet, Gallet & Cortet (2020) with forcing by oscillating cylinders, in Boury *et al.* (2021) with a trapezoidal domain forced by a wave generator or in Le Reun, Favier & Le Bars (2019) where the flow is excited by the elliptical instability. Moreover, the GM dominates other types of structures due to an inverse cascade that can lead to the formation of a condensate in which energy concentrates at the largest scale (Seshasayanan & Alexakis 2018). The GM influences the characteristics of the IWs to the point of scattering the inertia-gravity waves that are created when both rotation and stratification are present (Kafiabad, Savva & Vanneste 2019; Savva, Kafiabad & Vanneste 2021). Note that, even if 'geostrophic states are not universal to rotating turbulence' (Le Reun, Favier & Le Bars 2021), its structure at large scales has an important influence on the flow, and it is therefore essential to understand the mechanisms that feed and maintain this structure.

Nevertheless, the formation of the GM is not fully understood. It is consistent with the linear Taylor–Proudman theorem (Greenspan 1968), which states that in rapidly rotating flows in which an external slow time scale is imposed (e.g. a towed sphere) the flow is invariant along the vertical axis of rotation, i.e. its energy is concentrated in spectral regions where the wavevector has a vertical component $k_z = 0$ (Billant 2021). This theorem does not tell whether the resulting two-dimensional (2-D) flow has two or three velocity components in the general case. In addition, at moderate and small Rossby numbers ($Ro \lesssim 1$), the nonlinear energy redistribution tends to concentrate energy in the GM (i.e. $k_z \to 0$) as shown by DNS and by asymptotic theories (Cambon, Mansour & Godeferd 1997), both for decaying or forced rotating turbulence (Sharma, Verma & Sagar 2019).

The following different mechanisms are proposed to understand the emergence of the GM: (*a*) linear IW propagation as proposed by Davidson, Staplehurst & Dalziel (2006) who considered a cloud of turbulence and extended the argument to homogeneous turbulence in Staplehurst, Davidson & Dalziel (2008); (*b*) nonlinear mechanisms, for instance, studied by Smith & Waleffe (1999) who showed that the transfer of energy is driven by exactly resonant triadic interactions defined by

$$\boldsymbol{k} + \boldsymbol{p} + \boldsymbol{q} = 0 \quad \text{and} \quad \omega(\boldsymbol{k}) + \omega(\boldsymbol{p}) + \omega(\boldsymbol{q}) = 0, \tag{1.1}$$

where $\boldsymbol{k}, \boldsymbol{p}, \boldsymbol{q}$ are three-dimensional (3-D) wavevectors and $\omega(\boldsymbol{k})$ is the dispersion relation of an IW with wavevector $\boldsymbol{k}$. The wavenumber $k$ is defined as the modulus of the wavevector $\boldsymbol{k}$. These resonant triads accumulate energy in the spectral region with low ratio $k_z/k$ according to a statistical 'instability assumption' (Waleffe 1993), but they never reach exactly the GM or the horizontal plane $k_z = 0$ because the exact resonant interaction never involves this plane (also known as slow manifold): when $k_z = 0$, $\omega(\boldsymbol{k}) = 0$ with $\omega(\boldsymbol{q}) = -\omega(\boldsymbol{p})$ and $p_z = -q_z$ (Greenspan 1969; Waleffe 1993). Similarly, the asymptotic

weak turbulence theory (Bellet *et al.* 2006) excludes the possibility of a GM at a large-time limit at very low Rossby number $Ro \ll 1$. To reach $k_z = 0$, two other mechanisms can bypass Greenspan's analysis and transfer energy to the GM (Newell 1969; Smith & Waleffe 1999).

The first mechanism is due to near resonant triad interactions $p + q + k$ with $p_z = -q_z$, $k_z = 0$ and $\omega(p) + \omega(q) + \omega(k) \sim 0$. In Le Reun *et al.* (2020) an instability mechanism is shown numerically and analytically to excite the GM by IWs. It is driven by near resonant triadic interaction.

The second mechanism explained in Smith & Waleffe (1999) can be a quartetic interaction mechanism. The resonant quartet occurs when two successive triad interactions occur, leading to $k + p + q = 0$, $\omega(p) + \omega(q) + \omega(k) = 0$ and $p + r + s + t = 0$ and $\omega(p) + \omega(r) + \omega(s) + \omega(t) = 0$, where $k, p, q, r, s$ are 3-D wavevectors and $t$ is a 2-D wavevector representing the GM (i.e. $t_z = 0$). In Newell (1969) a quartetic mechanism is also introduced so that a resonant quartet of Rossby waves can transfer energy to a zonal flow. In Brunet *et al.* (2020) it is a quartetic secondary instability that is evoked to be responsible for the emergence of the GM. Indeed, experiments seem to show that the resonant quartets of IW can trigger an instability at the origin of the GM (Brunet *et al.* 2020) when rotating turbulence is dominated by IWs in the wave turbulence regime at low Rossby number.

These different mechanisms concern the emergence of the GM due to wave/wave interactions in the rotating fluid at low Reynolds number. In homogeneous rotating turbulence where both direct and inverse cascades exist, Mininni, Alexakis & Pouquet (2009) show the emergence of the GM alongside the presence of small eddies. van Kan & Alexakis (2020) showed that the transition from a flow without inverse energy cascade to a flow with an inverse energy cascade depends on the elongation of the domain. Buzzicotti, Di Leoni & Biferale (2018*b*) found that the presence of the GM ('slow' manifold) is essential for the formation of a stationary inverse cascade that feeds the GM. The 3-D mode ('fast' manifolds) plays a non-trivial role in bringing energy to the larger scales as well. In the work by Bourouiba, Straub & Waite (2012), the horizontal component of the GM is driven by the interaction of two small-scale horizontal GM and small 3-D components of fast manifolds. Buzzicotti *et al.* (2018*a*) found that the inverse cascade is generated by homochiral interactions that couple the 3-D fast mode and the GM. In these last two studies, a backward cascade is not a simple 2-D process but it is also due to non-trivial 3-D interactions at different scales. However, these analysis are based on the slow manifold (GM) and the rest of the flow is considered as the fast manifold. This part of the flow motion is composed of waves and eddies that must be considered separately in order to assess precisely their influence on and interaction with the GM. With this in mind, one has to address the following questions pertaining to the dynamics of rotating strong turbulence: in the presence of waves and eddies, what interactions transfer energy to the GM? Among wave/wave, wave/eddy, eddy/eddy or self-interactions, which one mostly drives the GM dynamics? At what scale do these interactions occur?

In order to answer these questions, we run direct numerical simulations (DNS) of rotating homogeneous turbulence in which we extract separately eddies, IWs and the GM. We adapt to rotating flows the separation technique of waves and eddies in stably stratified flows presented in Lam, Delache & Godeferd (2020, 2021). There is however an important difference between the rotating and stratified turbulent flows, because the spatial-based wave/eddy decomposition proposed by Riley, Metcalfe & Weissman (1981) in the stratified case does not exist in the rotating one.

In what follows, we first present the governing equation and the numerical framework in § 2. In this section we also expose the method used to separate waves and eddies in rotating turbulence and applied to 3-D fields coming from DNS. In § 3 we explore the different regimes of rotating turbulence explored by DNS: from a regime where waves dominate the flow to a regime where waves and eddies coexist. The energetics and energy fluxes in the flow considered as a system are analysed in § 4 and typical scales of interactions are discussed in § 5. Conclusions are drawn in § 6.

## 2. Extracting waves, eddies and GM in rotating turbulence

### 2.1. *Governing equations*

We consider an incompressible flow in a rotating frame, and by using the rotation formulation of the momentum equation, the corresponding Navier–Stokes equations are

$$\partial_t \boldsymbol{u} + \boldsymbol{\omega} \times \boldsymbol{u} = -\nabla p + \nu \nabla^2 \boldsymbol{u} - 2\boldsymbol{\Omega} \times \boldsymbol{u} + \boldsymbol{F} - \alpha \boldsymbol{u}^g, \tag{2.1}$$

$$\nabla \cdot \boldsymbol{u} = 0, \tag{2.2}$$

where $\boldsymbol{u} = (u_x, u_y, u_z)$ is the velocity vector, $\boldsymbol{\omega} = \nabla \times \boldsymbol{u}$ is the vorticity, $p$ is the modified pressure, $\nu$ is the kinematic viscosity and $\boldsymbol{\Omega} = (0, 0, \Omega)$ is the rotation rate along the vertical axis. The flow can be set in motion via the body force $\boldsymbol{F} = (F_x, F_y, F_z)$, which is a constant-power cylindrical forcing (see Maffioli, Delache & Godeferd 2020 and Maffioli 2017 for details). All equations and parameters are dimensionless by reference to *a priori* chosen length and time scales. To control the growth of the GM and prevent the formation of a condensate, a friction term $-\alpha \boldsymbol{u}^g$ is added (Le Reun *et al.* 2017), where $\boldsymbol{u}^g$ is the GM field. The GM velocity is defined as a velocity invariant along the vertical axis. In practice, it is computed from the inverse Fourier transform in space (noted $\mathscr{F}_{\boldsymbol{x}}^{-1}$) of the spatial Fourier modes (noted $\hat{\Box}$)

$$\boldsymbol{u}^g(\boldsymbol{x}, t) = \mathscr{F}_{\boldsymbol{x}}^{-1}[\hat{\boldsymbol{u}}(\boldsymbol{k}_h, k_z = 0, t)] \tag{2.3}$$

with coordinates of wavevector $\boldsymbol{k} = (k_x, k_y, k_z)$ and horizontal wavevector $\boldsymbol{k}_h = (k_x, k_y, 0)$. The GM is considered here as a whole as in Buzzicotti *et al.* (2018*b*) and not as in Buzzicotti *et al.* (2018*a*) and Bourouiba *et al.* (2012) where the GM is decomposed into two parts, a horizontal GM component and a vertical GM component.

Our method for extracting the IWs is based on their wave nature and their dispersion relation. Inertial waves are plane-wave solutions of the inviscid linearized Navier–Stokes equations, obtained by removing the nonlinear terms of (2.1) and identifying their dispersion relation

$$\omega_r(\boldsymbol{k}) = 2\Omega \frac{k_z}{k}. \tag{2.4}$$

The GM is also called slow mode or slow manifold because $\omega_r(k_x, k_y, k_z = 0) = 0$ (see, e.g. Smith & Waleffe (1999), Godeferd & Moisy (2015) or Buzzicotti *et al.* (2018*b*)). This dispersion relation $\omega_r(\boldsymbol{k})$ is modified in the presence of large-scale advection such as the GM. The sweeping effect of an IW by large structures, assimilated to an advecting velocity field $\boldsymbol{c}$, can be modelled by the following linearized equations:

$$\partial_t \boldsymbol{u}_L + \boldsymbol{c} \cdot \nabla \boldsymbol{u}_L = -\nabla p_L + \nu_L \nabla^2 \boldsymbol{u}_L - 2\boldsymbol{\Omega} \times \boldsymbol{u}_L + \boldsymbol{F}_L, \tag{2.5}$$

$$\nabla \cdot \boldsymbol{u}_L = 0 \tag{2.6}$$

Here $\boldsymbol{F}_L$ is the forcing and $\boldsymbol{u}_L$, $\nu_L$, $p_L$ are the velocity, viscosity and pressure of this model flow. In our modelling of the modification of IW's characteristics by a large-scale velocity

**971** A10-4

field, we do not take into account the refraction of waves by the GM ($\boldsymbol{u}_L \cdot \nabla \boldsymbol{c}$ term) since it does not significantly modify the dispersion relation with respect to the sweeping effect ($\boldsymbol{c} \cdot \nabla \boldsymbol{u}_L$ term), as shown by our preliminary numerical tests. Although $\boldsymbol{c}$ is expected to act in the two terms $\boldsymbol{u}_L \cdot \nabla \boldsymbol{c}$ and $\boldsymbol{c} \cdot \nabla \boldsymbol{u}_L$, the latter dominates when $\boldsymbol{c}$ is strong while the former dominates when $\boldsymbol{c}$ is both strong and at small scale (Lam 2021). Since the GM is a large-scale structure (see spectrum in figure 7), sweeping dominates over refraction and is the only term retained here.

The characteristics of the modified IWs are obtained by solving equations (2.5) and (2.6) and are used as a reference to extract the wave part from the full velocity obtained by (2.1) and (2.2). The mathematical formulation of the solutions of (2.1) and (2.5) is simpler if one uses polar-spherical coordinates, since, in Fourier space, incompressibility imposes that the velocity vector be perpendicular to the associated wavevector: $\nabla \cdot \boldsymbol{u} = 0 \Leftrightarrow \mathrm{i}\boldsymbol{k} \cdot \hat{\boldsymbol{u}} = 0$. This reference frame is also called Craya–Herring frame (Herring 1974; Sagaut & Cambon 2018). Its unit vectors are ($\boldsymbol{e}^t, \boldsymbol{e}^p, \boldsymbol{e}^k$) defined with respect to the rotation axis assumed to be along $\boldsymbol{z}$,

$$\boldsymbol{e}^t = \frac{\boldsymbol{k} \times \boldsymbol{z}}{|\boldsymbol{k} \times \boldsymbol{z}|}, \quad \boldsymbol{e}^p = \frac{\boldsymbol{k} \times (\boldsymbol{k} \times \boldsymbol{z})}{|\boldsymbol{k} \times (\boldsymbol{k} \times \boldsymbol{z})|}, \quad \boldsymbol{e}^k = \boldsymbol{k}/k. \tag{2.7a–c}$$

On this basis, the Fourier-transformed velocity writes $\hat{\boldsymbol{u}}(\boldsymbol{k}, t) = \hat{u}^t(\boldsymbol{k}, t)\boldsymbol{e}^t + \hat{u}^p(\boldsymbol{k}, t)\boldsymbol{e}^p$, where $\hat{u}^t$ and $\hat{u}^p$ are respectively the toroidal and poloidal velocities. By inverse Fourier transform of this spectral velocity, the physical velocity vector is thus expressed with only two independent components as $\boldsymbol{u}(\boldsymbol{x}, t) = \boldsymbol{u}^t(\boldsymbol{x}, t) + \boldsymbol{u}^p(\boldsymbol{x}, t)$ in the physical domain for velocity field; this expression is used for both (2.1) and (2.5). This description is used in the next § 2.2 to simply describe the IWs.

## 2.2. *Method of extraction of IWs*

As mentioned above, we adapt to rotating flows a decomposition technique previously applied in the stratified case to separate internal gravity waves and eddies (see Lam *et al.* 2021 and Lam 2021 for details). The reader will find in Lam (2021) details about the sweeping effect in the rotating case.

This technique consists of the following four steps.

(i) Direct numerical simulation of the nonlinear equations (2.1) and (2.2) to obtain the velocity fields $\boldsymbol{u}(\boldsymbol{x}, t)$ and extract the GM velocity field $\boldsymbol{u}^g(\boldsymbol{x}, t)$.
(ii) Direct numerical simulation of the linear equations (2.5) and (2.6) to obtain the IWs characteristics modified by the sweeping due to the GM velocity field, by taking $\boldsymbol{c}(\boldsymbol{x}, t) = \boldsymbol{u}^g(\boldsymbol{x}, t)$ obtained from step (i).
(iii) Building the $\zeta$ filter (defined in (2.9)) from the velocity field $\boldsymbol{u}_L(\boldsymbol{x}, t)$ obtained from step (ii).
(iv) Filtering the velocity fields $\boldsymbol{u}(\boldsymbol{x}, t)$ obtained by DNS in step (i) by using $\zeta$ obtained in (iii) to separate the wave part $\boldsymbol{u}^w(\boldsymbol{x}, t)$ and the eddy part $\boldsymbol{u}^e(\boldsymbol{x}, t)$.

Steps (i) and (ii) concern physical fields in space and time, whereas steps (iii) and (iv) operate in the four-dimensional (4-D) Fourier domain in space and time noted ($\boldsymbol{k}, \omega$), which is composed of the 3-D Fourier space defined by wavevector $\boldsymbol{k}$ and the one-dimensional frequency space $\omega$. This last step takes into account the space–time properties of waves and their transport by the advecting velocity $\boldsymbol{c}$. The processing in 4-D space is computationally expensive, as explained in § 3.2. In the following, we explain the details of steps (ii), (iii) and (iv).

When $c$ is homogeneous and constant, one can obtain all characteristics of IWs by computing an exact analytical solution of the Green's function associated with the linearized equations (2.5) and (2.6). This is done by using a forcing composed of Dirac functions in time and space $F_L = (0, 0, \delta(x)\delta(t))$, and solving (2.5) in the 4-D Fourier space in $(k, \omega)$, denoted $\tilde{\Box}$. The resulting analytical Green's function of IWs contains toroidal and poloidal components of velocity as

$$
\begin{pmatrix} \tilde{u}_L^t \\ \tilde{u}_L^p \end{pmatrix} = \begin{pmatrix} \frac{1}{2} \left\{ [\nu_L k^2 + i(\omega + c \cdot k - \omega_r(k))]^{-1} + [\nu_L k^2 + i(\omega + c \cdot k + \omega_r(k)]^{-1} \right\} \\ \frac{i}{2} \left\{ [\nu_L k^2 + i(\omega + c \cdot k - \omega_r(k))]^{-1} - [\nu_L k^2 + i(\omega + c \cdot k + \omega_r(k)]^{-1} \right\} \end{pmatrix},
$$
(2.8)

where $\omega_r(k)$ is the classical dispersion relation of IW ((2.4)). We observe from (2.8) that a peak of energy arises at the poles of the function when $\omega \to \pm\omega_r - c \cdot k$. This corresponds to the dispersion relation of IWs $\pm\omega_r$ modified by the sweeping effect $c \cdot k$ (see Lam *et al.* 2020 for details about the sweeping effect acting on waves).

We extend this analysis to an inhomogeneous advecting velocity $c(x, t) = u^g(x, t)$ such as the GM. Indeed, the search for the poles and, thus, the implicit dispersion relation is often used for waves other than IWs, when they are advected by a non-homogeneous mean flow and develop instabilities (see Huerre & Monkewitz 1990). This happens for unstable waves developing in Rayleigh–Bénard-Poiseuille flows (Carriere & Monkewitz 1999) or in weakly non-parallel shear flows (Monkewitz, Huerre & Chomaz 1993). In both cases, it is very difficult to obtain directly an analytical solution of the waves from the linear equations due to the non-homogeneity of the mean field. Different strategies are thus used such as the eigenfunction expansion method with a decoupling of the vertical (direction of inhomogeneity) and horizontal (Carriere & Monkewitz 1999) or the Wentzel–Kramers–Brillouin–Jeffreys method assuming a slow spatial variation of the weak non-parallelism and, thus, of the dispersion relation (Monkewitz *et al.* 1993). In both examples, it is possible to pass from $\omega$ frequencies to time $t$ by the residuals method (Huerre & Monkewitz 1990) taking into account appropriate integration contours where only poles contribute to integration. These authors' solutions reveal that the poles and, thus, the dispersion relation are central to approximate an explicit solution of the waves by using the residue theorem. In our case, the GM is slowly variable in time and in the horizontal plane and homogeneous in the vertical direction. We are therefore in a situation close to the above-mentioned flows. When passing from $(k, \omega)$ to $(x, t)$ by the fast Fourier transforms (FFTs), the presence of the poles dominates the FFT integrals. Since we cannot perform analytical development and in accordance with the literature described above, the poles should dominate the solutions in physical space as in the classical residue calculation. Moreover, our tests on DNS of Green's function have shown that the peak selection of Green's functions retains most of the energy compared with the total Green's function.

In order to filter out the wave part, we first solve the Green's function numerically and the solution for IWs of the linearized equations (2.5) and (2.6) with an inhomogeneous velocity $c(x, t) = u^g(x, t)$ by forcing via superimposed random Dirac functions in time and space. We force only the toroidal component of the flow by decomposing $F_L = F_L^t e^t + F_L^p e^p$ into toroidal and poloidal parts, and imposing $F_L^p = 0$ and $F_L^t$ as a sum of random Dirac functions (details in § 3.2). As the toroidal and poloidal components of IWs exchange energy with one another (Sagaut & Cambon 2018; Lam 2021), one can decide arbitrarily to force only the toroidal component of velocity, and let the linear system respond to this solicitation as a poloidal component and, thus, form the components of

a wave. Thus, we make sure to force only waves and not eddies that can have poloidal and toroidal components that are not defined by IWs. We could also have forced only the poloidal component. Secondly, in this new set of DNS, the wave part is defined from spectral regions where energy peaks (by virtue of (2.8)), and the remaining flow motion is assigned to the eddy part. Hence, the wave filter $\zeta(\boldsymbol{k}, \omega)$ is defined as

$$\text{if } |\tilde{u}_L^t(\boldsymbol{k}, \omega)|^2 \geq \beta^{-1} \max_\omega |\tilde{u}_L^t(\boldsymbol{k}, \omega)|^2 \text{ then } \zeta(\boldsymbol{k}, \omega) = 1 \text{ else } \zeta(\boldsymbol{k}, \omega) = 0, \quad (2.9)$$

where $\beta = 100$ is arbitrarily chosen so that the peaks of energy are assigned to wave motion (numerical details in § 3.2). Here $\zeta(\boldsymbol{k}, \omega) = 1$ is therefore indicative of areas in the $(\boldsymbol{k}, \omega)$ space where kinetic energy is highly concentrated, corresponding to the wave part of the flow, and $\zeta(\boldsymbol{k}, \omega) = 0$ for the eddy part. Compared with the stratified case (Lam *et al.* 2021), the forcing used to create the filter $\zeta(\boldsymbol{k}, \omega)$ stems from the toroidal term only, and results in a filter applied on both toroidal and poloidal components due to the fact that IWs are expected to be represented both in the toroidal and poloidal velocity components.

Thirdly, the filter $\zeta(\boldsymbol{k}, \omega)$ is applied to the data of the original DNS of (2.1). One obtains the wave $\tilde{\boldsymbol{u}}^w$, eddy $\tilde{\boldsymbol{u}}^e$ and GM $\tilde{\boldsymbol{u}}^g$ parts of the velocity field as

$$\text{for } k_z \neq 0: \quad \tilde{\boldsymbol{u}}^w(\boldsymbol{k}, \omega) = \zeta(\boldsymbol{k}, \omega)(\tilde{u}^t(\boldsymbol{k}, \omega)\boldsymbol{e}^t + \tilde{u}^p(\boldsymbol{k}, \omega)\boldsymbol{e}^p), \quad (2.10)$$

$$\text{for } k_z \neq 0: \quad \tilde{\boldsymbol{u}}^e(\boldsymbol{k}, \omega) = (1 - \zeta(\boldsymbol{k}, \omega))(\tilde{u}^t(\boldsymbol{k}, \omega)\boldsymbol{e}^t + \tilde{u}^p(\boldsymbol{k}, \omega)\boldsymbol{e}^p), \quad (2.11)$$

$$\text{for } k_z = 0: \quad \tilde{\boldsymbol{u}}^g(\boldsymbol{k}, \omega) = \tilde{\boldsymbol{u}}(k_h, k_z = 0, \omega), \quad (2.12)$$

$$\text{for all } \boldsymbol{k}: \quad \tilde{\boldsymbol{u}}(\boldsymbol{k}, \omega) = \tilde{\boldsymbol{u}}^g(\boldsymbol{k}, \omega) + \tilde{\boldsymbol{u}}^w(\boldsymbol{k}, \omega) + \tilde{\boldsymbol{u}}^e(\boldsymbol{k}, \omega). \quad (2.13)$$

We finally apply the inverse 4-D Fourier transform from frequency space $(\boldsymbol{k}, \omega)$ to physical space $(\boldsymbol{x}, t)$ for each part: $\boldsymbol{u}^l(\boldsymbol{x}, t) = \sum_{\boldsymbol{k}, \omega} \tilde{\boldsymbol{u}}^l(\boldsymbol{k}, \omega) e^{-i\boldsymbol{k} \cdot \boldsymbol{x} - i\omega t}$, where $l$ stands for $w$, $e$ or $g$. The velocity field $\boldsymbol{u}(\boldsymbol{x}, t)$ is thus explicitly split in wave, eddy and GM parts as

$$\boldsymbol{u}(\boldsymbol{x}, t) = \boldsymbol{u}^g(\boldsymbol{x}, t) + \boldsymbol{u}^w(\boldsymbol{x}, t) + \boldsymbol{u}^e(\boldsymbol{x}, t). \quad (2.14)$$

Note that we use the term 'eddy part' for convenience, admitting that it is initially defined by what it is not: they are not waves. It is possible to compare the spatial decomposition of Buzzicotti *et al.* (2018*a*) with our spatiotemporal decomposition (2.14): their slow part is identified with our GM part ($g$) and their fast part is identified with our wave part ($w$) and our eddy part ($e$).

As done in Lam *et al.* (2021), this decomposition permits to define an orthogonal basis and an inner product in vector function space, by using the complete set of unit vector functions $e^{i\boldsymbol{k} \cdot \boldsymbol{x}}$ and $e^{i\omega t}$.

Considering two functions $\hat{f}$ and $\hat{g}$, one can define an inner product in terms of wavevector $\boldsymbol{k}$ and time $t$, as

$$[\hat{f}(\boldsymbol{k}, t), \hat{g}(\boldsymbol{k}', t)] \equiv \frac{1}{T} \int_T \hat{f}(\boldsymbol{k}, t)\overline{\hat{g}(\boldsymbol{k}', t)}\delta_{\boldsymbol{k}-\boldsymbol{k}'} \, dt, \quad (2.15)$$

where $T$ is the considered time span and $\overline{\square}$ is the complex conjugate. Due to the orthogonality of vector space functions and orthogonality of Fourier velocity with wavevector space $\boldsymbol{k}$ from incompressibility, one shows the orthogonality between wave, eddy and GM parts,

$$[\hat{u}_m^i(\boldsymbol{k}, t), \hat{u}_n^j(\boldsymbol{k}', t)] \neq 0 \quad \text{only if } i = j \text{ and } \boldsymbol{k} = \boldsymbol{k}', \quad (2.16)$$

where $i, j$ stand for $w$, $e$ or $g$, and $m, n$ stand for space direction $x$, $y$ or $z$. This provides a way to calculate the overall energy content and the energy content in a sphere of radius $K$,

defined respectively by

$$\langle \hat{\boldsymbol{u}}^i, \hat{\boldsymbol{u}}^j \rangle = \sum_{\substack{\boldsymbol{k} \\ m=x,y,z}} Re[\hat{u}_m^i(\boldsymbol{k}, t), \hat{u}_m^j(\boldsymbol{k}, t)], \tag{2.17}$$

$$\langle \hat{\boldsymbol{u}}^i, \hat{\boldsymbol{u}}^j \rangle_K = \sum_{\substack{|\boldsymbol{k}|=K \\ m=x,y,z}} Re[\hat{u}_m^i(\boldsymbol{k}, t), \hat{u}_m^j(\boldsymbol{k}, t)]. \tag{2.18}$$

## 3. Exploration of different flow regimes

### 3.1. *Rotating turbulence regimes*

Different regimes for rotating flows can be observed according to Godeferd & Moisy (2015). In general, these regimes are usually defined by the Rossby number $Ro_l = U/(2\Omega l)$ and the Reynolds number $Re_l = Ul/\nu$, where $U$ is a velocity scale associated with an integral scale $l$, $\nu$ is the kinematic viscosity and $2\Omega$ is the rotation rate. At $Ro_l \ll 1$ and $Re_l \ll 1$ the flow is dominated by IWs. For $Ro_l \ll 1$ and $Re_l > 1$, the flow is dominated by IWs that interact weakly and lead to the wave turbulence regime. For $Ro_l < 1$ and $Re_l \gg 1$, quasi-2-D turbulence is observed. This calls for the definition of the horizontal Reynolds number $Re_h = U_h^4/\varepsilon\nu$, where $U_h$ is defined hereafter. However, in our numerical simulations we control the emergence of the GM and the flow is less dominated by the 2-D flow at low Rossby number even if its importance increases as $Ro$ decreases, defined hereafter in (3.1). Yet, the flow is still dominated by the GM in terms of kinetic energy, and therefore, its motion remains mostly horizontal, although not entirely at all scales. We account for this by refining the description of the phenomenological properties by introducing the inertial Reynolds number $Re_I$ (Marino *et al.* 2013) and another horizontal Rossby number $Ro$ using a horizontal velocity scale and the dissipation, thus avoiding the introduction of a specific length scale among multiple possible ones. By using the kinetic energy dissipation or energy injection rate $\varepsilon$ as a control parameter in turbulent state, it leads to the definition of the parameters $Re_I$ and $Ro$ defined by

$$Ro = \frac{\varepsilon}{2\Omega U_h^2} \quad \text{and} \quad Re_I = \frac{\varepsilon}{\nu(2\Omega)^2}, \tag{3.1a,b}$$

where $U_h = u_h - u_h^g$ is the root mean square (r.m.s.) of the horizontal velocity field $u_h$ without the r.m.s. of the GM horizontal velocity $u_h^g$.

Using $\varepsilon$ has the advantage that all non-dimensional numbers are linked to the turbulent state without any indeterminacy linked to the choice of length scale in the turbulent case. Nevertheless, the definition of these parameters can be rewritten by approximating the kinetic energy dissipation. Indeed, $\varepsilon$ represents the energy that is injected by forcing directly the wave and eddy parts, avoiding the GM. When the rotation is strong, the imprint of the GM is characterized by a maximum elongation in the vertical direction ($k_z = 0$) and a horizontal length separating the different tubes forming the GM. It influences the structure of the flow, so that its characteristic scale becomes the horizontal length $L_f$. Here $L_f$ can also be estimated by the horizontal forcing scale ($L_f = 2\pi/k_h$ with the horizontal forcing frequency $k_h \sim 1$ in our numerical simulations). Moreover, at large scale, the horizontal velocity of fluctuation is larger than the vertical velocity as shown in experiments by Campagne *et al.* (2015), the mean velocity is then associated to horizontal velocity $U_h$ from which the velocity of the GM has been removed. As in stratified turbulence (Maffioli, Brethouwer & Lindborg 2016), we use $\varepsilon \sim U_h^3/L_f$ and in
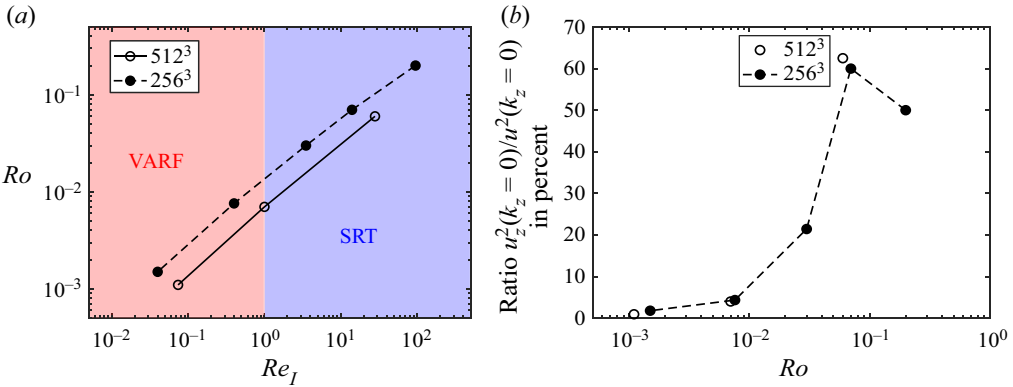
Figure 1. (*a*) Parameters of the numerical simulations in the Rossby and inertial Reynolds plane. Viscosity-affected rotating flow (VARF): regime where waves interact weakly and rotation strongly influences all scales. Strongly rotating turbulence (SRT): regime where rotation strongly influences the large scales (up to $l_\Omega$) and weakly influences the small scales (from $l_\Omega$ down to the dissipative scale $\eta$). (*b*) Relative amount of the vertical GM energy $u_z^2(k_z = 0)$ over the total GM energy $u^2(k_z = 0)$. Open circles are for numerical simulations with $512^3$ points and filled circles for $256^3$ points.

that case we find that $Ro = U_h/(2\Omega L_f)$, which is the horizontal Rossby number and $Re_I = U_h^3/((2\Omega)^2\nu L_f)$. As in stratified turbulence in which a buoyancy Reynolds number can be defined from Froude and Reynolds numbers (Brethouwer *et al.* 2007), the non-dimensional numbers in rotating flows are related by $Re_I = Re_h Ro^2$, where $Re_h = U_h^4/\varepsilon\nu$ is the horizontal Reynolds number that can be rewritten as $Re_h = U_h L_f/\nu$ using $\varepsilon \sim U_h^3/L_f$. Here $Re_I$ appears as the ratio of inertial forces to viscous and Coriolis forces, but can also be defined as the ratio $Re_I = (l_\Omega/\eta)^{4/3}$ of the Kolmogorov length scale $\eta = (\varepsilon/\nu^3)^{-1/4}$ – the smallest scale in the turbulent flow – to the Zeman–Hopfinger scale $l_\Omega = \sqrt{\varepsilon/(2\Omega)^3}$ that separates large scales strongly influenced by the Coriolis force from smaller inertial scales (Mory & Hopfinger 1985; Zeman 1994). Consequently, the introduction of $Re_I$ instead of $Re_l$ opens the way to a refined phenomenological description. At large inertial Reynolds numbers $Re_I \gg 1$, IWs dominate the large scales until scale $l_\Omega$, and a classical inertial sub-range can occur from scale $l_\Omega$ to the dissipative scale $\eta$ where isotropy is restored. In contrast, at low $Re_I \ll 1$, the Coriolis force dominates the flow and all scales are dominated by the Coriolis force and the IWs up to $l_\Omega$, without lending space to a classical inertial sub-range. This is the regime of wave turbulence where the dissipation is carried out by waves and the scale of dissipation is no longer $\eta$. This phenomenology is less clear when examined in view of $Re_l$ than on $Re_I$, which permits us to assess regimes wherein eddies or IWs are expected to dominate. Additional phenomenologies of rotating flows can be conveyed by other non-dimensional parameters, such as the Ekman number $E_k = Ro/Re_h$ (Mininni *et al.* 2009) for bounded flows, as in planetary cores (Le Bars 2016).

Our simulations explore the high rotation rate regime at $Ro \ll 1$ with different values of $Re_I$. They are focused on the transition from a regime called viscosity-affected rotating flow (VARF) where waves interact weakly and rotation strongly influences all scales, i.e. $Ro \ll 1$ and $Re_I \ll 1$, to a regime called strongly rotating turbulence (SRT) where rotation strongly influences large scales (up to $l_\Omega$) and weakly influences small scales (from $l_\Omega$ to $\eta$), i.e. $Ro \ll 1$ and $Re_I \gg 1$. These regimes are named in a manner similar to the regimes observed in stratified turbulence by Brethouwer *et al.* (2007). We illustrate the transition between these two regimes in figure 1(*a*). According to Godeferd & Moisy (2015), the VARF regime includes the wave turbulence regime and IW regime since all

waves dominate the regime. On the other hand, the SRT regime includes the quasi-2-D turbulence.

In order to quantify the effect of rotation versus inertia on the GM, we introduce a specific Rossby number based on the GM: $Ro^g = u^g/(L^g 2\Omega)$. Here $u^g$ is the r.m.s. velocity of the GM and the characteristic length of the GM is $L^g = 2\pi$ because the GM is defined as invariant vertically ($k_z = 0$) and the size of the box of the different numerical simulations is $2\pi$.

### 3.2. *Numerical setting and parameters*

We solve the Navier–Stokes equations (2.1)–(2.2) using a standard pseudo-spectral algorithm in a $2\pi$-periodic 3-D spatial domain. A phase-shifting method is used to treat aliasing in the nonlinear term (see Lam *et al.* 2020 for details). Eight numerical simulations have been run with the parameters shown in table 1 at resolutions of $256^3$ and $512^3$ points. The exploration of parameters is mainly based on $256^3$ points, the higher resolution of $512^3$ points is used to confirm the trends at increasing resolution. As shown in figure 1(*a*), by changing the resolution, it is possible to explore a small variation of one parameter by keeping the other constant to evaluate variation tendencies. For instance, for $2\Omega = 80$, $Ro \simeq 0.007$ and $Re_I$ change from 0.4 to 1 when the resolution changes from $256^3$ to $512^3$ points.

The Taylor-length-based Reynolds number is $Re_\lambda = u_{rms}\lambda/\nu$, with $\lambda$ the Taylor scale and $u_{rms}$ the r.m.s. velocity as shown in table 1. The global Rossby numbers $Ro$ and $Ro^g$ are much smaller than 1, which indicates that the rotation effects are important both globally and for the GM.

In numerical simulations, when energy condensates at large scales, a linear frictional damping is added as in classical 2-D turbulence (Boffetta & Ecke 2012). Le Reun *et al.* (2017) and Buzzicotti *et al.* (2018*a*) use this technique in rotating fluid to mimic the interaction of the GM with boundaries and control its growth. Furthermore, adding something to dissipate the GM has also been done in experiment, for instance, by Monsalve *et al.* (2020) with a honeycomb grid installed at the top and bottom of a rotating tank in order to 'fully suppress spontaneous energy transfers to GMs'. In our DNS, the value of $\alpha$ in the friction term $-\alpha u^g$ is set to $\alpha = 0.5$. It stabilizes the GM in rotating turbulence and the ratio of GM energy over total energy $E^g/E^t$ shown in table 1, where $E^g(t) = \int u^g(x, t)^2 \, dx^3$ and $E^t(t) = \int u(x, t)^2 \, dx^3$, has the same order of magnitude (between 6.8 % and 15 % despite the difficulty of predicting this percentage before carrying out the simulation). For $\alpha = 0.5$, the added dissipation on the GM is strong and the GM accounts only for about 10 % of the total energy in the flow.

The forcing $F$ is localized on a cylindrical spectral surface of horizontal wavenumber $k_h = 1$ and range of vertical wavenumber $2 \le k_z \le 4$, away from the GM. This is similar to Maffioli *et al.* (2020) and Lam *et al.* (2021) where the forcing is set in stratified turbulence to avoid the shear mode that plays a role similar to the GM in rotating flows. The injected power $P = \int F \cdot u \, dv$ is constant during time to reach a statistically stationary state but varies for each case (see table 1). The value of kinematic dissipation $\varepsilon$ (defined in § 4.3) is not equal to the value of $P$ in table 1 because $\varepsilon$ does not include the added viscosity. Hence, our largest Reynolds number DNS require us to adjust $P$ in order to retain maximum $\varepsilon$ while maintaining $k_{max}\eta \gtrsim 1$, where $k_{max}$ is the maximum wavenumber in the DNS.

The side DNS that solve the linear equations (2.5) and (2.6) can be run with parameters different than the main DNS for nonlinear equations (2.1) and (2.2). For instance, their viscosity is chosen negligible ($\nu = 10^{-8}$) so that energy peaks are sharper (see (2.8)) and, consequently, the wave filter selectivity is more accurate. The toroidal forcing $F_L^t$ in the

| $2\Omega$ | $Ro$ | $Re_l$ | $Re_h$ | $Ek$ | $Re_\lambda$ | $Ro^g$ | $1/l_\Omega$ | $P$ | $\varepsilon$ | $E^g/E^t$ | $\omega_{max}$ | $\omega_{min}$ | $k_{max}\eta$ |
|---|---|---|---|---|---|---|---|---|---|---|---|---|---|
| | | | | | $512^3$ points, $\nu = 1/700$ and $\alpha = 0.5$ | | | | | | | | |
| 15 | 0.06 | 28 | 7780 | $7.7 \times 10^{-6}$ | 255 | 0.014 | 19 | 10 | 9 | 8.9 | 520 | 1.0 | 1.02 |
| 80 | 0.007 | 1 | 20 400 | $3.4 \times 10^{-7}$ | 720 | 0.06 | 240 | 14 | 7 | 16 | 980 | 2.0 | 1.09 |
| 300 | 0.0011 | 0.074 | 61 200 | $1.8 \times 10^{-8}$ | 1350 | 0.0022 | 1400 | 20 | 9.5 | 15.6 | 1570 | 3.1 | 1.01 |
| | | | | | $256^3$ points, $\nu = 1/250$ and $\alpha = 0.5$ | | | | | | | | |
| 5 | 0.2 | 95 | 1960 | $1.1 \times 10^{-4}$ | 120 | 0.036 | 3.6 | 10 | 9.5 | 6.8 | 200 | 0.4 | 1.10 |
| 15 | 0.07 | 14 | 2860 | $2.5 \times 10^{-5}$ | 150 | 0.015 | 16 | 14 | 13 | 8.1 | 630 | 1.3 | 1.01 |
| 30 | 0.03 | 3.5 | 3900 | $7.7 \times 10^{-6}$ | 210 | 0.0096 | 47 | 14 | 12.5 | 8.2 | 790 | 1.6 | 1.02 |
| 80 | 0.0076 | 0.4 | 6930 | $1.1 \times 10^{-6}$ | 395 | 0.006 | 230 | 14 | 10 | 15 | 790 | 1.6 | 1.08 |
| 300 | 0.0015 | 0.04 | 17 800 | $8.4 \times 10^{-8}$ | 600 | 0.0019 | 1400 | 20 | 14 | 11.4 | 1050 | 2.1 | 0.99 |

Table 1. List of parameters in the DNS runs. These parameters are defined and discussed in the text. The ratio $E^g/E^t$ is done in percent %.

side linear DNS is

$$F_L^t(\boldsymbol{x}, t) = \begin{cases} \delta(\boldsymbol{x}(t)) & \text{if } t \le 100\Delta t, \\ 0 & \text{otherwise,} \end{cases} \tag{3.2}$$

where $\Delta t$ is the time step of the linear DNS, $\delta(\boldsymbol{x}(t))$ is the Dirac function in space and $\boldsymbol{x}(t)$ is randomly defined at each time step $\Delta t$. In the full DNS, we use a small time step $\Delta t$ to match the Courant–Friedrichs–Lewy constraint, but the time step $\Delta t'$ for the 4-D Fourier transform can be larger ($\Delta t' > \Delta t$). The 4-D algorithm is applied to 1000 3-D fields at successive time steps $\Delta t'$. Although data are obtained for 1000 time steps, the different statistics are only taken over a duration of $600\Delta t'$, in order to avoid the cutoff oscillations at the edges of the time interval (Lam *et al.* 2020). The time step $\Delta t'$ imposes the minimum and maximum resolved pulsation $\omega_{max} = \pi/\Delta t'$ and $\omega_{min} = 2\pi/(1000\Delta t')$, which are respectively the largest and smallest pulsations in the 4-D method (see values in table 1). The maximum frequency $\omega_{max}$ takes into account the sweeping effect on the smallest scale $\eta$ (or largest wavenumber $k_\eta = 1/\eta$), i.e. $\omega_{max} \gtrsim 2\Omega + c_{rms}(k_z = 0)k_\eta$, where $c_{rms}(k_z = 0)$ is the average value of the r.m.s. velocity of the GM.

Note that the advecting velocity $c$ is also updated every $\Delta t'$. No windowing technique is used during the process except for the definition of the filter $\zeta$. Not using windowing prevents a change of the energy of wave and eddy parts, as well as the modification of the overall energetic content.

For identifying the spectral peaks in the Green's function, the same value of the cutoff parameter $\beta = 100$ is used for all simulation of Green's function (2.5). This choice of $\beta$ has already been detailed in Lam *et al.* (2021) where it ensures that most of the energy in (2.9) is considered as waves (around 90 %) and most peaks in (2.8) are also considered as waves. This value comes from several previous attempts, and is a tradeoff between lower $\beta$ that would lead to wrongly selecting waves as eddies, and larger beta where eddies would wrongly be selected as waves.

In practice, the cost of the present two-stage separation technique is rather large because it requires us to run two DNS, in addition to the 4-D Fourier transform. It also requires storage of a large number of 3-D fields. This currently limits the approach to relatively moderate resolutions, although it permits us to obtain significantly original results in the following. It is also possible to apply the separation algorithm directly to the velocities in the Cartesian frame. The accuracy is expected to be similar, but the computational cost would be larger since the filtering would be applied on three components ($u_x, u_y, u_z$) instead of two ($u^t, u^p$).

Figure 1(*a*) shows the different regimes of our DNS in the ($Ro,Re_I$) parameter plane. With respect to $256^3$ simulations, $512^3$ numerical simulations permit us to slightly increase $Ro$ while keeping $Re_I$ constant, or to slightly decrease $Re_I$ while keeping $Ro$ constant. The figure also shows that we explore the transition between the VARF and the SRT regimes.

Moreover, we deal in this paper with a non-elongated domain height $H$ compared with the energy injection $l_{in}$ at large scale in our DNS (i.e. $h = H/l_{in} \sim 1$). The Rossby number is chosen small ($Ro \ll 1$, see table 1) and, according to van Kan & Alexakis (2020) (their figure 11), our simulations are in a split cascade domain. This means that our simulations contain both an inverse and a forward energy cascade, even if we force the large scale (see Buzzicotti *et al.* 2018*a* run B).

Table 2 shows the different time scales of waves $T^w = 2\pi/(2\Omega)$, eddies $T^e = L^e/u^e$ and GM $T^g = L^g/u^g$ with $L^g = 2\pi$ as the GM is invariant in the vertical axis ($k_z = 0$) and $u^g$ is the r.m.s. velocity of the GM. The time scale of eddies is computed from the integral length scale $L^e$ (eddies are assumed to be three dimensional) and the r.m.s velocity of eddies $u^e$.

| $2\Omega$ | $256^3$ points, $\nu = 1/250$ | | | $512^3$ points, $\nu = 1/700$ | | |
|---|---|---|---|---|---|---|
| | $T^w$ | $T^e$ | $T^g$ | $T^w$ | $T^e$ | $T^g$ |
| 5 | 1.257 | 0.0944 | 5.581 | — | — | — |
| 15 | 0.419 | 0.0847 | 4.385 | 0.419 | 0.0946 | 4.805 |
| 30 | 0.209 | 0.0879 | 3.588 | — | — | — |
| 80 | 0.0785 | 0.1027 | 2.077 | 0.0785 | 0.1002 | 2.071 |
| 300 | 0.0209 | 0.0827 | 1.793 | 0.0209 | 0.0843 | 1.484 |

Table 2. Time scale of the wave ($T^w$), eddy ($T^e$) and GM ($T^g$) part of the flow.

We observe that even if the GM is a result of the spatial filter of the flow (i.e. $k_z = 0$), its time scale is different than that of the waves and eddies: we always have $T^g \gg T^e, T^w$ and the time scale of the GM is always the slowest. Moreover, the time scale of eddies is roughly constant for all simulations $T^e \sim 0.1$. The time scale of wave $T^w$ could be larger or smaller than $T^e$ because $T^w$ evolves as a function of the rotating rate $2\Omega$. Note that, by using our method, the eddy and wave parts are separated both spatially and temporally: some wave and eddy terms can share a similar spatial scale but not the same frequency, or a similar temporal scale but not the same wavevector.

Movies of the time-evolving vertical velocity of total, wave and eddy fields for the $512^3$ points numerical simulation and $2\Omega = 80$ or $2\Omega = 15$ can be seen in supplementary materials available at https://doi.org/10.1017/jfm.2023.644. We have chosen to visualize our flow by animations because it is difficult to see large-scale waves with a snapshot. The wave part of our decomposition shows waves with large-scale oscillations, which is the signature of the waves that dominate the large scale and the mark of the GMs that have stable positions. In contrast, the eddy part of our decomposition shows small scales and eddies oscillating around the GM.

## 4. Energy and flux for waves, eddies and GM

### 4.1. *Energies*

The above orthogonal decomposition of velocity permits us to decompose the total energy $E^T = \langle \hat{\boldsymbol{u}}, \hat{\boldsymbol{u}} \rangle / 2$ into energies assigned to the wave, eddy and GM parts: $E^T = E^w + E^e + E^g$, with $E^l = \langle \hat{\boldsymbol{u}}^l, \hat{\boldsymbol{u}}^l \rangle / 2$ for $l = w, e, g$.

The velocity of the GM defined in (2.3) is *a priori* three component, but its vertical component $\hat{u}_z^g$ varies most with the physical parameters. This is illustrated in figure 1(*b*) that shows the ratio of GM vertical energy $\langle \hat{u}_z^g, \hat{u}_z^g \rangle$ over its horizontal energy $\langle \hat{u}_x^g, \hat{u}_x^g \rangle + \langle \hat{u}_y^g, \hat{u}_y^g \rangle$. The vertical energy can reach 60 % of the total energy at $Ro \simeq 0.07$, but it decreases quickly with $Ro$. Overall, the GM has to be considered as a 3-D flow.

Figure 2 shows $E^g / E^T$, the amount of GM energy in percentage of the total energy depending on the inertial Reynolds number $Re_I$ (figure 2*a*) and the Rossby number $Ro$ (figure 2*b*). The figure shows that $E^g$ varies between 7 % and 16 % of the total energy (data also in table 1). It also shows that the percentage of GM energy increases when either $Re_I$ or $Ro$ decreases.

Figure 2 also compares the wave energy $E^w$ and eddy energy $E^e$ against their sum (also $E^T - E^g$), i.e. the flow energy regardless of GM energy. In this way we assess the wave/eddy energy partition independently of the importance of the GM. The figure indicates that the energy is mainly stored in the wave part. When $Ro$ or $Re_I$ increases, the
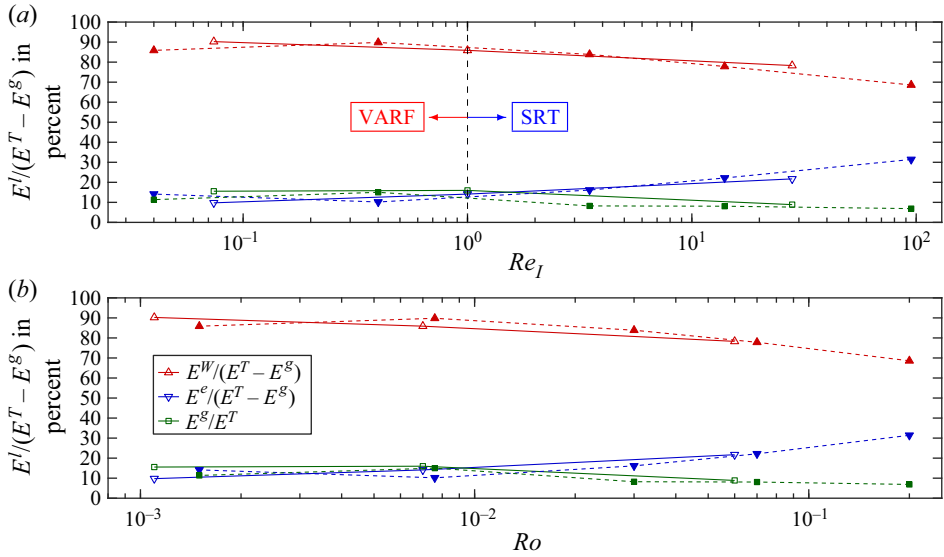
Figure 2. Evolution of the percentage energy $E^l/(E^T - E^g)$ for waves ($l = w$) and eddies ($l = e$) and evolution of the percentage of GM energy ($E^g/E^T$) against (*a*) $Re_I$, (*b*) $Ro$. Numerical simulations with $512^3$ points are shown with open symbols and solid lines, and numerical simulations with $256^3$ points are shown with filled symbols and dotted lines.

wave energy decreases from $\simeq 90\,\%$ to $\simeq 70\,\%$ of $(E^T - E^g)$, and the eddy energy increases by the same amount.

### 4.2. *Balance of energy and flux*

The evolution of total energy in rotating turbulence is driven by the flux of energy in the equation $dE^T/dt = P - \varepsilon^T$, where $\varepsilon^T$ is the total dissipation including the added dissipation term on the GM. During the statistically stationary regime when $dE^T/dt \sim 0$, the production $P$ is in equilibrium with the total dissipation $P \sim \varepsilon^T$. We propose hereafter to use the wave/eddy decomposition to address the question about how do wave-, eddy- and GM-related fluxes evolve with rotation?

To do this, we compute a Lin-type equation for the two-point space correlation of waves, eddies and GM velocities. This is achieved by projecting the Fourier-transformed equation (2.1) on the velocity $\hat{u}^l(\boldsymbol{k}, t)$ of the $l = w, e, g$ part, using the inner product $[\widehat{(2.1)}, \hat{u}^l(\boldsymbol{k}, t)]$. We then symmetrize by adding the complex conjugate, before computing the energy density within a sphere of radius $K$, which is $\langle \widehat{(2.1)}, \hat{u}^l(\boldsymbol{k}, t) \rangle_K$. Due to the orthogonality property (2.16) between parts, we obtain the separate energy balance equations for each of the waves, eddies and GM, depending on the wavenumber $K$, as

$$\partial_t e^w(K) = \sum_{i=w,e,g} t_{iw}^w(K) + t_{ie}^w(K) + t_{ig}^w(K) - 2\nu K^2 e^w(K) + p^w(K), \tag{4.1}$$

$$\partial_t e^e(K) = \sum_{i=w,e,g} t_{iw}^e(K) + t_{ie}^e(K) + t_{ig}^e(K) - 2\nu K^2 e^e(K) + p^e(K), \tag{4.2}$$

$$\partial_t e^g(K) = \sum_{i=w,e,g} t_{iw}^g(K) + t_{ie}^g(K) + t_{ig}^g(K) - 2\nu K^2 e^g(K) - 2\alpha e^g(K), \tag{4.3}$$

**971** A10-14

where, for each part $l$, $e^l(K) = \langle \hat{\boldsymbol{u}}, \hat{\boldsymbol{u}}^l \rangle_K$ is its kinetic energy density, $p^l(K) = \langle \hat{\boldsymbol{F}}, \hat{\boldsymbol{u}}^l \rangle_K$ is the forcing and $t_{ij}^l(K) = -\langle \widehat{\boldsymbol{\omega}^i \times \boldsymbol{u}^j}, \hat{\boldsymbol{u}}^l \rangle_K$ represents the energy transfers on part $l$ due to an interaction with part $j$ involving part $i$. Indeed, the triadic structure of quadratic nonlinearity can be expressed fundamentally in terms of a collection of triadic interactions such that $\boldsymbol{k} + \boldsymbol{p} + \boldsymbol{q} = 0$ where each triad checks

$$(\hat{\boldsymbol{\omega}}^i(\boldsymbol{q}) \times \hat{\boldsymbol{u}}^j(\boldsymbol{p})) \cdot \hat{\boldsymbol{u}}^l(\boldsymbol{k}) = -(\hat{\boldsymbol{\omega}}^i(\boldsymbol{q}) \times \hat{\boldsymbol{u}}^l(\boldsymbol{k})) \cdot \hat{\boldsymbol{u}}^j(\boldsymbol{p}), \tag{4.4}$$

interpreting as a mode-to-mode energy transfer rates where the wavevector $\boldsymbol{q}$ of part $i$ is the mediator mode that promotes the exchange of energy between wavevectors $\boldsymbol{p}$ of part $j$ and $\boldsymbol{k}$ of part $l$, much like a catalyst (see Verma 2019 for details and (A9) in Appendix A for demonstration (4.4).). Note that the rotation formulation of the momentum equation (2.1) shows that $\boldsymbol{\omega}$ has two roles: the rotation rate due to velocity for each point in physical space and the mediator mode for each scale in Fourier space.

This nonlinear term yields nine different interactions $(i, j) \in \{ww, we, ew, ee, wg, gw, eg, ge, gg\}$ for each of the three parts of the energy $l = w, e, g$, i.e. *a priori* a total of 27 transfers $t_{ij}^l$. Yet, all of these transfers are not physically possible. For instance, the interaction of two GMs cannot produce an eddy or wave: since the GM corresponds to $k_z = 0$, the interaction of two GMs can only create another GM, due to the triadic condition $-\boldsymbol{k} = \boldsymbol{p} + \boldsymbol{q}$.

The corresponding transfers are therefore $t_{gg}^e = t_{gg}^w = 0$. For the same reason, the interaction of a GM with a wave or eddy cannot produce a GM, since a wave or eddy component has a non-zero vertical wavenumber, and $t_{wg}^g = t_{gw}^g = t_{eg}^g = t_{ge}^g = 0$. Finally, there remains only 21 physically possible transfers: five of them take or give energy to the GM, eight transfers take or give to the wave part and eight to the eddy part. Summing over all wavenumbers $K$ in (4.1)–(4.3), we obtain the energy balance equation for each part, i.e.

$$\mathrm{d}E^w/\mathrm{d}t = T_{ee}^w + T_{we}^w + T_{wg}^w + T_{ge}^w + T_{eg}^w + \varepsilon^w + P^w, \tag{4.5}$$

$$\mathrm{d}E^e/\mathrm{d}t = T_{ww}^e + T_{ew}^e + T_{wg}^e + T_{gw}^e + T_{eg}^e + \varepsilon^e + P^e, \tag{4.6}$$

$$\mathrm{d}E^g/\mathrm{d}t = T_{ee}^g + T_{we}^g + T_{ww}^g + T_{ew}^g + \varepsilon^g, \tag{4.7}$$

where $E^l = \sum_K e^l(K) = \langle \boldsymbol{u}^l, \boldsymbol{u}^l \rangle$, $l = w, e, g$. The kinetic energy dissipations of waves and eddies are $\varepsilon^l = \nu \langle k^2 \hat{\boldsymbol{u}}^l, \hat{\boldsymbol{u}}^l \rangle$. The dissipation of the GM is the sum of the turbulent dissipation and the dissipation due to the added viscosity $\alpha$: $\varepsilon^g = \varepsilon^{\nu, g} + \varepsilon^{\alpha, g}$, with $\varepsilon^{\nu, g} = \nu \langle k^2 \hat{\boldsymbol{u}}^g, \hat{\boldsymbol{u}}^g \rangle$ and $\varepsilon^{\alpha, g} = \alpha \langle \hat{\boldsymbol{u}}^g, \hat{\boldsymbol{u}}^g \rangle$. The transfer terms are $T_{ij}^l = \sum_K t_{ij}^l(K) = -\langle \widehat{\boldsymbol{\omega}^i \times \boldsymbol{u}^j}, \hat{\boldsymbol{u}}^l \rangle$.

Again, the integrated energy transfer $T_{ij}^l$ over all triads taking into account (4.4) implies that the $i$ part is a catalyst for the energy exchange between the $j$ and $l$ parts.

Following Verma (2019) and our mode-to-mode energy transfer (4.4), the summed triadic transfers are such that $T_{ij}^l = -T_{il}^j$ (see Appendix A), and are also exchange terms between the different parts. Doing so, the mediator has gone from being a mediator between the scales to a mediator between the different parts $j$ and $l$.

Moreover, this equality implies that $T_{ij}^j = 0$ and then, in the 21 transfer terms, seven conservative transfer terms are such that namely $T_{gg}^g = T_{ww}^w = T_{ee}^e = T_{ge}^e = T_{we}^e = T_{gw}^w = T_{ew}^w = 0$. The conservative terms $T_{ij}^j = 0$ are thus similar to convection terms for a passive scalar, since they convey the modification of part $j$ helped by part $i$ that acts onto part $j$.

**971** A10-15

For instance, $t_{ew}^w$ can be phenomenologically interpreted as waves propagating at the periphery of a vortex, as illustrated in a rotating and stratified fluid (Moulin & Flór 2006). Another instance is $t_{ee}^w$ that can be considered as a source of wave emission due to the mutual interaction of eddies. The $t_{ij}^l$ terms assess the importance of the interaction even though it is not yet identified as a given particular physical process (e.g. vortex stretching by large structures). To make this link would require us to analyse further the dynamical context of separate processes, but this is beyond the scope of this paper.

Finally, the other 14 transfer terms convey net energy exchanges such that $T_{ij}^l \neq 0$. Whereas conservative transfer terms such that $T_{ij}^j = 0$ modify the self-interaction of $j$ part with help of $i$ part, only net transfer terms $T_{ij}^l$ are able to bring the energy from $j$ part to $l$ part.

In § 4.3, we investigate further the net transfers where all conservative terms disappear, whereas in § 5 we discuss specifically the characteristics of the GM cascade when all terms remain, as in (4.3), which is the main aim of this paper.

### 4.3. *A global description of net transfer*

Due to their number, the 14 terms of net transfer $T_{ij}^l$ render the analysis of (4.5)–(4.7) difficult. We choose to analyse them via a flow diagram, also called Sankey diagram in which transfers are represented by arrows of width proportional to their intensity. This permits us to identify the most important transfers or fluxes in the dynamical system.

Figure 3 shows Sankey diagrams representing the three balance equations for the three higher resolution simulations. The Sankey diagram can be understood as a hydraulic line. The input of the hydraulic line is the forcing power $P = P^w + P^e$ and the equivalent of the output of the hydraulic line are the different dissipative terms $\varepsilon^w$, $\varepsilon^e$ and $\varepsilon^g$. The transfer terms $T_{ij}^l$ take or bring energy to one of the parts of our flow decomposition and can be associated to different pipes in a hydraulic line. This diagram helps us to visualize quantitatively (4.5)–(4.7) and the energy fluxes from the injection $P$ to the three dissipations $\varepsilon^w$, $\varepsilon^e$ and $\varepsilon^g$ either directly or indirectly by exchange terms $T_{ij}^l$. Of course, although the diagram does not show them explicitly, scales can be associated to the different terms: injection mostly concerns large scales and dissipation small ones.

The width of each band is proportional to the importance of each flux it represents. Red, blue and green indicate respectively the wave, eddy and GM parts. The colour of the exchange part between the terms $T_{ij}^l$ and $T_{il}^j = -T_{ij}^l$ has the mixed colour of parts $l$ and $j$. For each part $l = w, e, g$, white boxes $B^l$ indicate the sum of positive transfers $T_{ij}^l > 0$ (input) to the left of the box and negative transfers $T_{ij}^l < 0$ (output) to the right of the box. The forcing $P^l$ feeds directly the input balance of energy $B^l$ and all the dissipation $\varepsilon^l$ dissipates the energy from the output balance of energy $B^l$. Since no forcing goes to the GM, boxes $B^g$ help us to find the origin of the transfer from the GM to eddies or to waves. Since our simulations are almost, but not exactly, in a statistically stationary state, a small flux remains that represents the residual $dE^l/dt$ terms. The unsteady terms appear almost negligible except the wave part $dE^w/dt$, especially at smallest $Ro = 0.0011$ and $Re_I = 0.074$, which means a regime dominated by waves. These small unsteady terms indicate that the wave tank is emptying. These terms could come from the period of waves at $\omega \sim 0$ that is too large to be taken into account in the expensive post processing. Nevertheless, it is reasonable to assume that these terms will not change the trends that are largely captured.
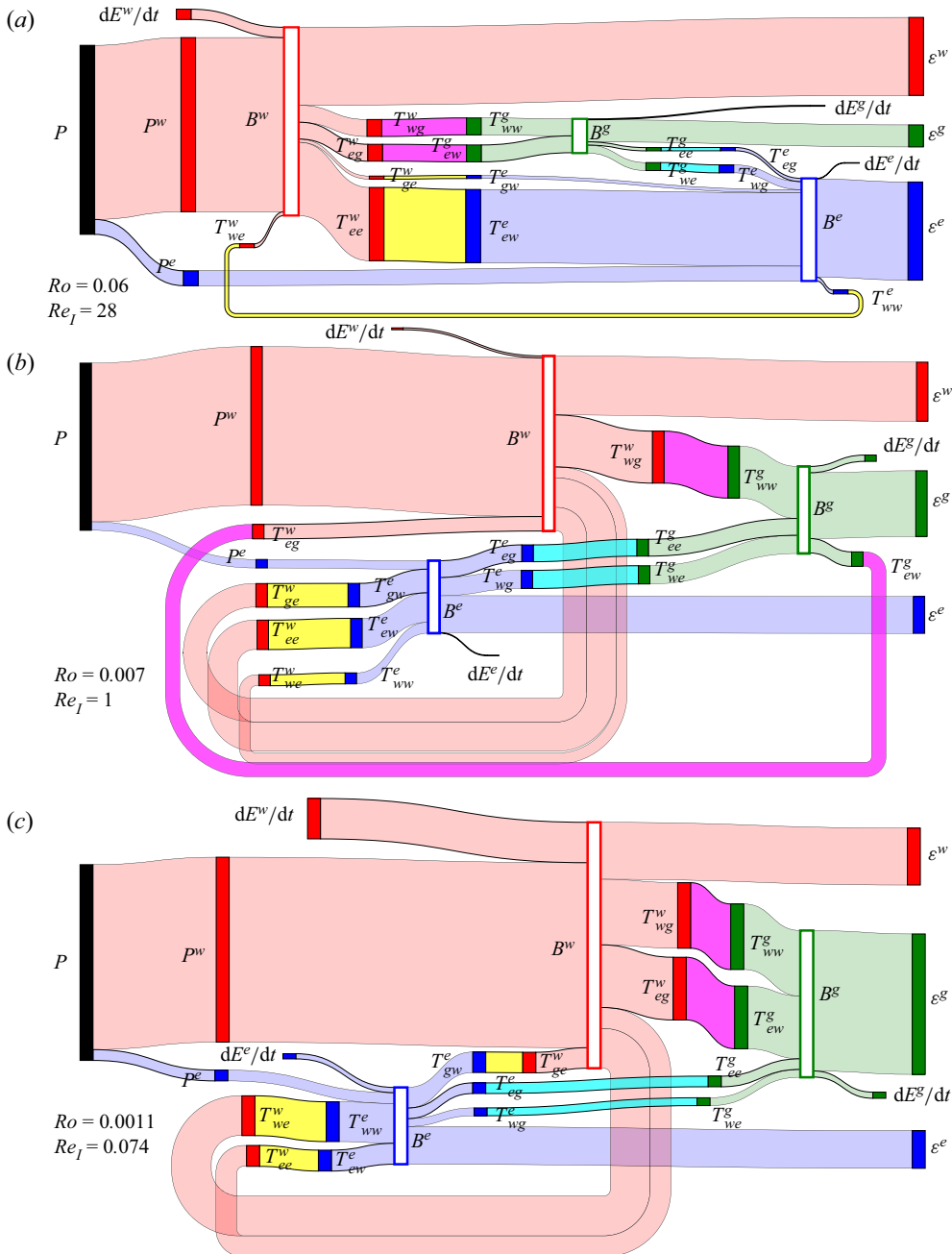
**971** A10-16

Figure 3. Sankey diagrams representing the different terms in (4.5)–(4.7) for the three numerical simulations at resolution $512^3$ points. The three DNS correspond to the indicated Rossby and inertial Reynolds numbers. The boxes $B^l$ (with $l = w, e, g$) represent the input/output balance of energy for any part $l$. Colours indicate input energy $P$ (black), waves (red), eddies (blue), GM (green), transfer between waves and the GM (magenta), eddies and the GM (cyan) and waves and eddies (yellow).
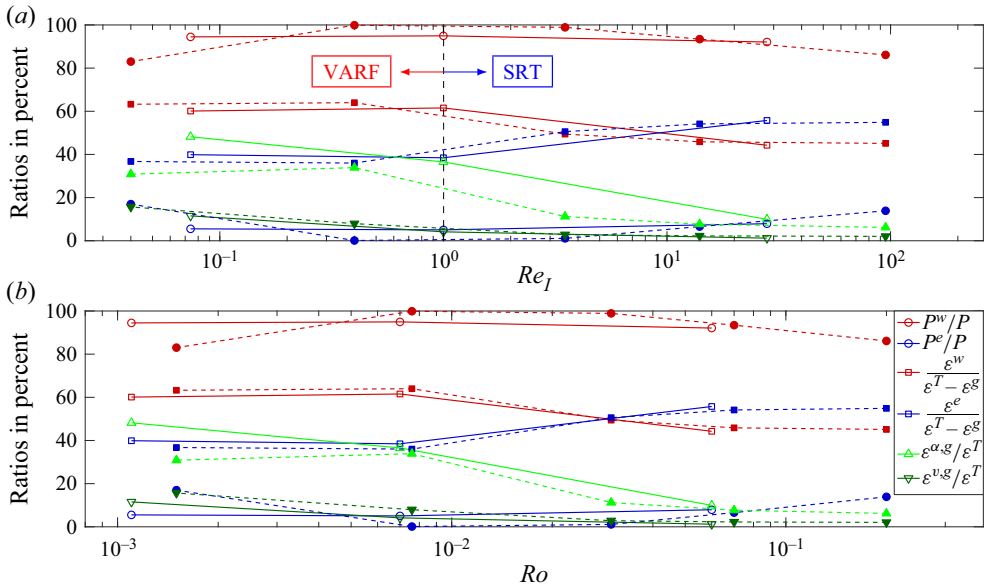
Figure 4. Ratio of forcing $P^l/P$ and ratio of dissipation against the total dissipation without the GM $\varepsilon^l/(\varepsilon^T - \varepsilon^g)$ for waves ($l = w$) and eddies ($l = e$). Ratio of dissipation of the GM due to the added viscosity term on the GM ($\varepsilon^{\alpha,g}/\varepsilon^T$) and the kinetic dissipation $\varepsilon^{\nu,g}/\varepsilon^T$ against total dissipation. Results are shown against (*a*) $Re_I$, (*b*) $Ro$. Open symbols and solid lines are DNS with $512^3$ points, filled symbols and dotted lines are DNS with $256^3$ points.

For the sake of clarity, we analyse, for example, the case of the Sankey diagram with $Ro = 0.06$ and $Re_I = 28$. First we note that all terms have their relative importance shown by the size of the bar. We start from the forcing input $P$ (in black). This represents the amount of energy that is inserted in the flow. This energy is then distributed in a wave part (forcing on waves $P^w$, in red) and an eddy part (forcing on eddies $P^e$, in blue). This energy can then be directly associated to the white coloured boxes $B^l$ (which represent the balance of input/output of energy). Then, transfers ($T_{ij}^l$) occur: energy is taken from one balance of energy $B^l$ to another balance of energy $B^j$. For example, $T_{ee}^w$ pumps energy from waves (the box $B^w$) and gives it to eddies ($B^e$) through the transfer $T_{ew}^e$. This can be explained as we have $T_{ee}^w = -T_{ew}^e$. Finally the energy is dissipated by waves ($\varepsilon^w$), eddies ($\varepsilon^e$) and the GM ($\varepsilon^g$). Hence, from this Sankey diagram, one can observe all transfers occurring from one component of the flow to another one, and its relative importance. For example, in that case, the transfers $T_{ww}^e$, $T_{gw}^e$ and $T_{eg}^e$ are negligible compared with other transfers. The most important transfers are $T_{ew}^w$, $T_{ww}^g$ and $T_{ew}^g$.

We now discuss the flow dynamics depending on the regime characterized by the inertial Reynolds and the Rossby numbers. We use Sankey diagrams (figure 3) to better understand the multiple interactions between different flow parts, along with curves showing the evolution of production and dissipation with respect to these two non-dimensional numbers (figure 4). Figure 4 shows the dependence with $Re_I$ and $Ro$ of the percent amount of forcing into waves $P^w/P$ and eddies $P^e/P$ – where the total injected power is $P = P^w + P^e$ – and of the dissipations $\varepsilon^{w,e}/(\varepsilon^T - \varepsilon^g)$, $\varepsilon^{\alpha,g}/\varepsilon^T$ and $\varepsilon^{\nu,g}/\varepsilon^T$, where $\varepsilon^g = \varepsilon^{\nu,g} + \varepsilon^{\alpha,g}$ is the total dissipation of the GM and $\varepsilon^T = \varepsilon^w + \varepsilon^e + \varepsilon^g$ is the total dissipation. As noted above for the energies, the figure shows that most of the forcing goes into waves ($P^w/P > 80\%$) whereas little forcing goes into eddies ($P^e/P < 20\%$).
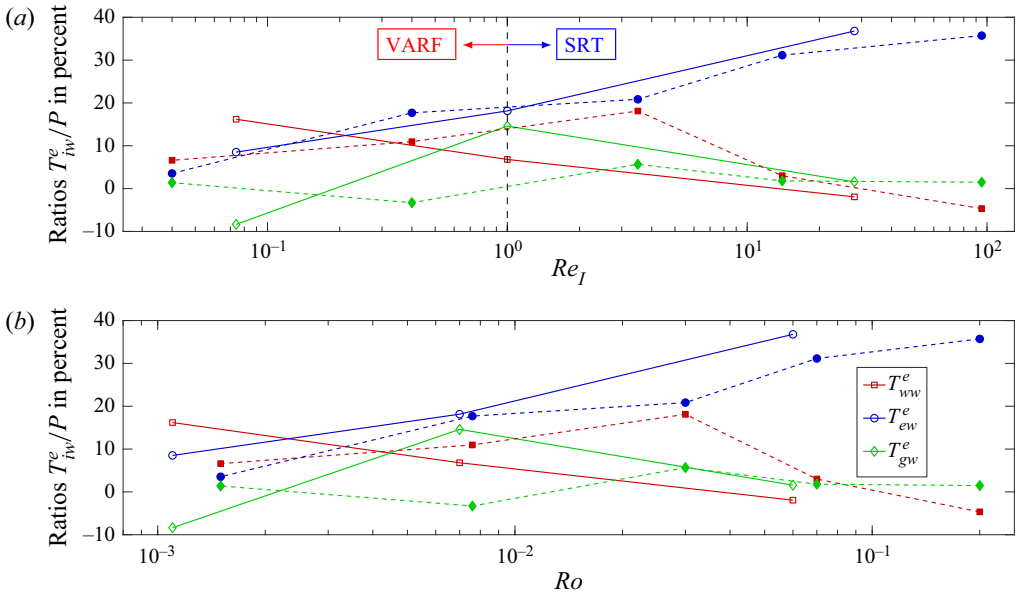
**971** A10-18

Figure 5. Evolution of the global transfer from waves to eddies divided by forcing $P$ against (*a*) $Re_I$, (*b*) $Ro$. Open symbols and solid lines are DNS with $512^3$ points, filled symbols and dotted lines are DNS with $256^3$ points.

However, figure 4 shows that the different dissipations $\varepsilon^w$, $\varepsilon^e$ and $\varepsilon^g$ are not distributed in the same proportions as the different forcing terms $P^w$, $P^e$. This attests that interactions between each part redistribute the energies: since the GM does not directly receive power from the forcing, the two parts of the GM dissipation $\varepsilon^{v,g}$, $\varepsilon^{\alpha,g}$ are divided by the total dissipation $\varepsilon^T$, to estimate their relative amounts. Note that the total kinetic energy dissipation used to define the Rossby and inertial Reynolds numbers in (3.1) is defined without added viscosity, i.e. $\varepsilon = \varepsilon^w + \varepsilon^e + \varepsilon^{v,g}$. It appears that most of the dissipation due to the GM is due to the added viscous term $\alpha$ since $\varepsilon^{v,g} < \varepsilon^{\alpha,g}$. Moreover, when increasing $Re_I$ at constant $Ro$ or when decreasing $Ro$ at constant $Re_I$, the kinetic energy dissipation $\varepsilon^{v,g}$ and the added dissipation $\varepsilon^{\alpha,g}$ of the GM decreases. At the same time, the two other dissipations for the wave and eddy $\varepsilon^w$, $\varepsilon^e$ share the remaining part of the dissipation $\varepsilon^r = \varepsilon^T - \varepsilon^g$: at low $Ro$ and $Re_I$, $\varepsilon^w \simeq 60\,\%\,\varepsilon^r > \varepsilon^e \simeq 40\,\%\,\varepsilon^r$ and at higher $Ro$ and $Re_I$, $\varepsilon^e \simeq 55\,\%\,\varepsilon^r > \varepsilon^w \simeq 45\,\%\,\varepsilon^r$. This evolution of dissipation from a wave-dominated regime to a more eddy-dominated regime is expected. However, although the input power is mainly into waves, the high levels of dissipation of the eddy part and of the GM suggest that a net transfer from the wave part occurs. For the sake of simplicity, in the following, we will focus on the transfers from waves to eddies or to the GM.

We consider the balance equation (4.6) for $E^e$, in which the three net transfers from waves to eddies are $T^e_{ww}$, $T^e_{ew}$ and $T^e_{gw}$. These transfers are plotted in figure 5 and illustrated on the Sankey diagram in figure 3. Since different numerical simulations correspond to a different forcing power $P$ and different relative values of $T^l_{ij}$, we rather represent the transfers as a fraction of $P$. The figure shows that the net transfer from an eddy/wave interaction $T^e_{ew}$ is always strong for all cases and increases with $Re_I$. The other transfers $T^e_{gw}$ and $T^e_{ww}$ fluctuate, with no clear trend. The transfer from a wave/wave interaction $T^e_{ww}$ is larger at low $Re_I$ and $Ro$, and decreases with $Re_I$ and $Ro$. The physical mechanism that
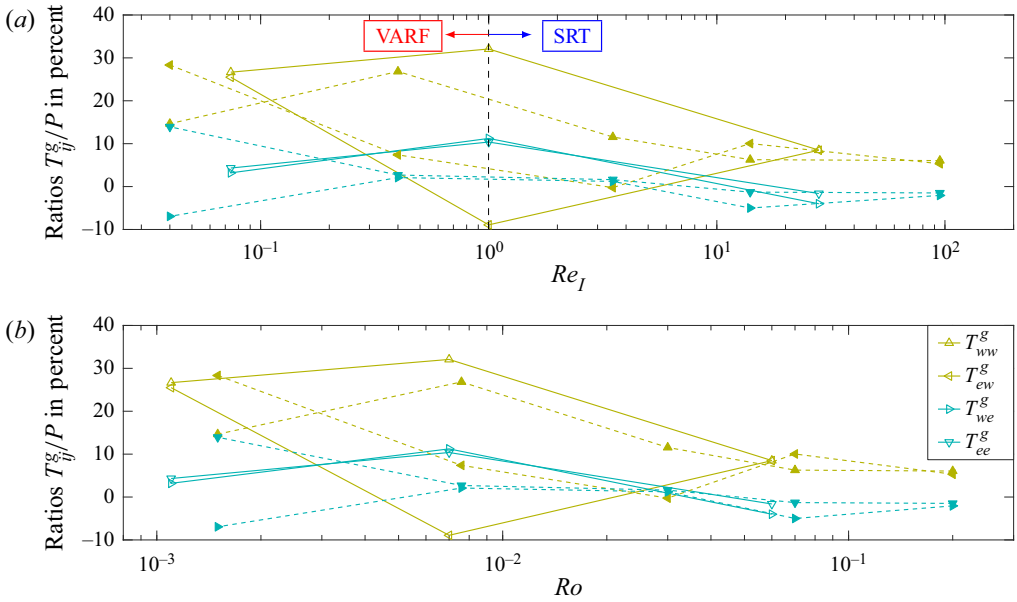
Figure 6. Evolution of the transfers from waves or eddies to the GM divided by forcing $P$ against (*a*) $Re_I$, (*b*) $Ro$. Numerical simulations with $512^3$ points are shown with open symbols and solid lines, and numerical simulations with $256^3$ points are shown with filled symbols and dotted lines.

produces such a transfer may be linked to a wave breaking mechanism (Moulin & Flór 2005).

In the balance equation (4.7) for $E^g$, $T^g_{ew}$ and $T^g_{ww}$ are net transfers from waves (*w*) to the GM (*g*) helped by eddies (*e*) and waves (*w*) respectively. $T^g_{ee}$ and $T^g_{we}$ are net transfers from eddies to the GM helped by eddies and waves, respectively. Their evolutions with $Re_I$ and $Ro$ are plotted in figure 6. A significant amount of energy is transferred from the wave part to the GM by the wave/wave interaction term $T^g_{ww}$ that dominates all net transfers. This wave/wave interaction $T^g_{ww}$ is consistent with mechanisms found by Brunet *et al.* (2020) or Le Reun *et al.* (2020) in the wave turbulence regime. In our simulations it seems to still be present in a turbulent regime at higher $Re_I$. Surprisingly, the eddy/wave interaction $T^g_{ew}$ and eddy/eddy interaction $T^g_{ee}$ can still play an important role in the transfer of energy to the GM from waves and from eddies. In particular, at highest $Re_I$ or lowest $Re_I$, the eddy/wave interaction $T^g_{ew}$ is of the same order of magnitude as the wave/wave interaction $T^g_{ww}$. This is illustrated on the Sankey diagrams in figures 3(*a*) at $Re_I = 28$ and 3(*c*) at $Re_I = 0.074$. At $Re_I \simeq 1$ (figure 3*b*), the eddy/wave interaction $T^g_{ew}$ pumps energy from the GM whereas the eddy/eddy interaction $T^g_{ee}$ and the wave/eddy interaction $T^g_{we}$ give energy to the GM from an eddy component.

## 5. Scale-by-scale analysis of supply process of GM

### 5.1. *Characterisation of GM transfers*

In this section we focus on the scale-by-scale characterization of the GM and, more specifically, on the typical scales at which interactions with the GM occur. The kinetic energy of the GM at wavenumber $K$ is $e^g(K) = \langle \hat{\boldsymbol{u}}, \hat{\boldsymbol{u}}^g \rangle_K$ and is shown in figure 7(*a*) for the different numerical simulations at resolution $512^3$ points. One observes that the inertial
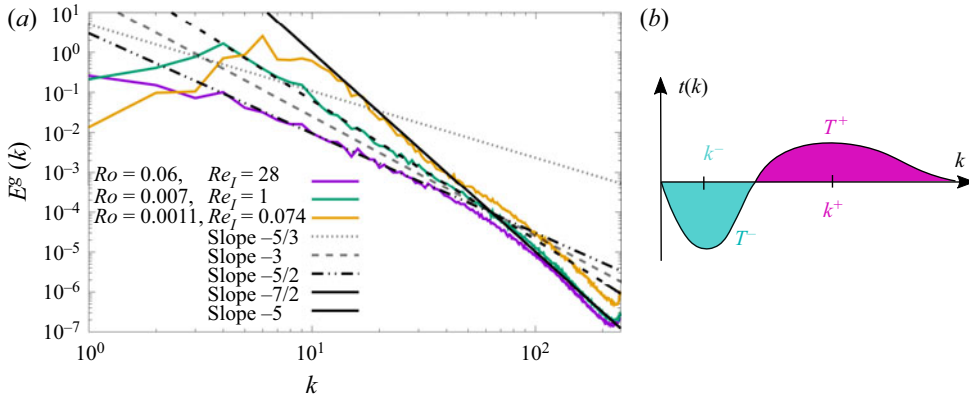
Figure 7. (*a*) Energy spectra of the GM for various runs at the specified Rossby and inertial Reynolds numbers. Typical power laws are indicated for reference. (*b*) An idealized transfer reduced in four variables $T^+$, $T^-$, $k^+$, $k^-$.

ranges of these $e^g(K)$ spectra can be fitted with different power laws depending on the regime, ranging from $K^{-5}$ to $K^{-5/2}$ when $Re_I$ or $Ro$ increase. The GM energy spectra computed by Buzzicotti *et al.* (2018*a*) were found to scale as $K^{-3}$. No such power law appears exactly in our simulations, but it is in between the scalings obtained at $Ro = 0.06$, $Re_I = 28$ and $Ro = 0.007$, $Re_I = 1$. This is consistent with our observation that the GM power law decreases when the flow is more turbulent and has less waves.

Using simplifications detailed in §4.2, (4.3) for the GM energy spectrum can be written as

$$\partial_t e^g(K) = t^g_{ee}(K) + t^g_{we}(K) + t^g_{ww}(K) + t^g_{ew}(K) + t^g_{gg}(K) - 2(K^2\nu + \alpha)e^g(K). \quad (5.1)$$

Summing over all $K$, one obtains again the equation for net transfer (4.7). In (5.1), $t^g_{gg}$ is a conservative term reflecting self-interactions of the GM, whereas other terms are net transfer terms with the wave or eddy. By comparison, Bourouiba *et al.* (2012) obtain a similar equation for spectral energy budgets for the horizontal component of the GM and vertical component of the GM but they only take into account the interaction with the 3-D modes or fast manifold, without decomposition into wave and eddy contents. The interaction that feeds the GM is thus reduced to two interactions: a self-interaction of the GM and an interaction of the GM with fast manifolds. A similar decomposition is applied in Buzzicotti *et al.* (2018*a*) for the total energy. The wave/eddy decomposition exhibits five interactions for the GM and expresses all the possible kinds of interactions. In particular, the terms $t^g_{ww}$, $t^g_{ew}$ represent the exchange of energy between the wave and GM helped respectively by wave and eddy parts, whereas $t^g_{we}$ and $t^g_{ee}$ represent the exchange of energy between the eddy and GM helped respectively by wave and eddy parts.

We now analyse the evolution of the GM and related net transfers or conservative transfers with reference to a typical transfer schematically represented in figure 7(*b*). Such a transfer can be characterized with the following four quantities:

(i) $T^{+,g}_{ij} = \sum_{k,t^g_{ij}(k)>0} t^g_{ij}(k)$, the total value of transfer given to $g$ by the interaction with $j$ and helped by $i$;

(ii) $T_{ij}^{-,g} = \sum_{k,t_{ij}^g(k)<0} t_{ij}^g(k)$, the total value of transfer pumped from $g$ by the interaction with $j$ and helped by $i$;

(iii) $k_{ij}^{+,g} = \sum_{k,t_{ij}^g(k)>0}(k\,t_{ij}^g(k)/T_{ij}^{+,g})$, the weighted average scale of transfer given to $g$ by the interaction with $j$ and helped by $i$;

(iv) $k_{ij}^{-,g} = \sum_{k,t_{ij}^g(k)<0}(k\,t_{ij}^g(k)/T_{ij}^{-,g})$, the weighted average scale of transfer pumped from $g$ by the interaction with $j$ and helped by $i$.

Our proposed representation is simplified and leads to the cancellation of some terms for different wavevectors $\boldsymbol{k}$ sharing the same wavenumber $k$. Despite this simplification, the proposed representation can help us understand global trends (direct or inverse cascade, importance of the transfer...). A different choice of scale could be made, for example, by looking for the scale that maximizes the subgrid cross-field transfer based on the subgrid tensor and by using a filtering approach as in large-eddy simulations (Eyink & Aluie 2009). This could permit us to characterize precisely the scale of the cascade process that is a local interaction. Note that the local or non-local nature of the interactions is not explored here, although it would be interesting to perform this analysis on the interaction terms.

Each interaction verifies that $T_{ij}^g = T_{ij}^{+,g} + T_{ij}^{-,g}$ and $T_{gg}^{+,g} = -T_{gg}^{-,g}$ for the particular case of a conservative term $T_{gg}^g = 0$. The difference between values of $T_{ij}^{+,g}$ and $T_{ij}^{-,g}$ indicates the strength of the interaction, whereas the values of $k_{ij}^{+,g}$ and $k_{ij}^{-,g}$ indicate the typical scales of this interaction.

When $T_{ij}^{+,g} \gg 0$ and $T_{ij}^{-,g} \sim 0$, energy is given to the GM by part $j$ at a given scale $k_{ij}^{+,g}$; when $T_{ij}^{-,g} \ll 0$ and $T_{ij}^{+,g} \sim 0$, energy is pumped from the GM by part $j$ at a given scale $k_{ij}^{-,g}$. When $T_{ij}^{+,g} \gg 0$ and $T_{ij}^{-,g} \ll 0$, a refined analysis is called for: if $k_{ij}^{+,g} > k_{ij}^{-,g}$, energy is pumped at large scale and given at smaller scale; if $k_{ij}^{-,g} < k_{ij}^{+,g}$, energy is pumped at small scale and given at larger scale. This observation is usually associated with a direct or inverse cascade of the conservative transfer due to the fact that $T_{gg}^{+,g} = -T_{gg}^{-,g} \gg 0$. For the net transfer term, we extend this phenomenology and we refer to a direct or inverse net transfer between the $g$ part (GM) and $j$ part. The difference $|k_{ij}^{+,g} - k_{ij}^{-,g}|$ accounts for the strength of that cascade: the larger the difference, the stronger the direct or inverse cascade.

## 5.2. *Transfer from waves to GM*

The net transfer terms from waves to the GM are $T_{ww}^{+,g}$, $T_{ww}^{-,g}$, $T_{ew}^{+,g}$, $T_{ew}^{-,g}$ associated respectively with characteristic scales $k_{ww}^{+,g}$, $k_{ww}^{-,g}$, $k_{ew}^{+,g}$, $k_{ew}^{-,g}$. They are plotted in figure 8 against $Re_I$.

In § 4.3 we showed that the wave/wave interaction is the dominant interaction for supplying the GM. At all $Re_I$, figure 8 shows that $T_{ww}^{+,g} \gg |T_{ww}^{-,g}| \sim 0$ with a quasi constant scale $k_{ij}^{+,g} \simeq 5 - 6$. This means that wave/wave interactions give energy from waves to the GM at relatively large scale.

Regarding the eddy/wave interaction, a net transfer occurs from waves to the GM helped by eddies. According to figure 8, we confirm the results of § 4.3: at small and high $Re_I$, the eddy/wave interaction amplitudes are of the same order of magnitude as the wave/wave interaction, and the energy is pumped from waves $w$ to the GM $g$ helped by eddies $e$.
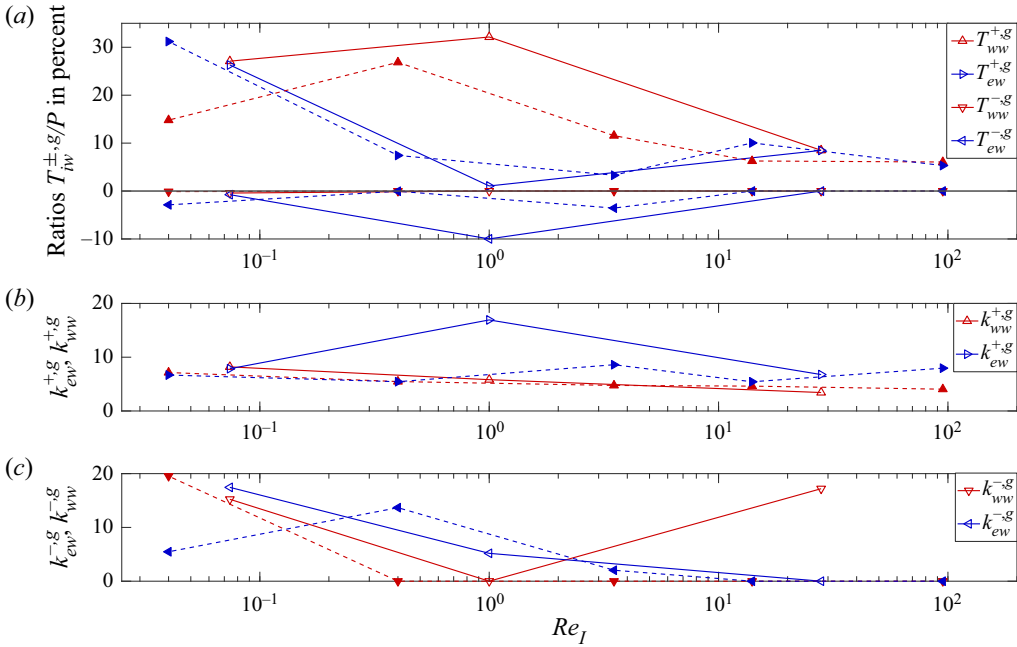
**971** A10-22

Figure 8. Evolution of the detailed transfer from waves to the GM against $Re_I$. Transfer amplitude divided by forcing $P$ is in ($a$), the average positive scale of transfer is in ($b$) and the average negative scale of transfer is in ($c$). Numerical simulations with $512^3$ points are shown with open symbols and solid lines, and numerical simulations with $256^3$ points are shown with filled symbols and dotted lines.

This eddy/wave interaction occurs at large scale, since $T_{ew}^{+,g} \gg |T_{ew}^{-,g}| \sim 0$ and $k_{ew}^{+,g} \simeq 5 - 6$. Furthermore, at a moderate inertial Reynolds number $Re_I \sim 1$, we confirm that the eddy/wave interaction pumps the energy from the GM to waves helped by eddies, the latter being relatively large-scale ones ($T_{ew}^{-,g} < 0$ and $k_{ew}^{-,g} \sim 5 - 9$). Nevertheless, a difference appears between $Re_I \simeq 1$ and $Re_I \simeq 3.5$ ($512^3$ and $256^3$ points): whereas at $Re_I \simeq 1$, no energy is given (i.e. $T_{ew}^{+,g} \simeq 0$), for $Re_I \simeq 3.5$, a significant part of energy is given from wave to GM at small scale associated to a direct net transfer (i.e. $T_{ew}^{+,g} \simeq |T_{ew}^{-,g}|$ and $k_{ew}^{+,g} \simeq 10 > k_{ew}^{-,g} \simeq 2$).

These results are consistent with those of Le Reun *et al.* (2020) and Brunet *et al.* (2020) where the physical processes that bring energy to the GM are based on wave/wave interactions. Yet, none of these studies assumes that an eddy/wave interaction can play a key role in the transfer of energy to the GM.

### 5.3. *Transfer from eddies to GM*

The net transfer terms from eddies to the GM are described by $T_{we}^{+,g}$, $T_{we}^{-,g}$, $T_{ee}^{+,g}$, $T_{ee}^{-,g}$ associated respectively with scales $k_{we}^{+,g}$, $k_{we}^{-,g}$, $k_{ee}^{+,g}$, $k_{ee}^{-,g}$. They are plotted against $Re_I$ in figure 9.

The eddy/eddy interaction, i.e. the transfer of energy from eddies to the GM helped by eddies, depends on $Re_I$. Confirming the results of § 4.3, at small $Re_I$, the eddies give energy to the GM, and this is done at large scale since $T_{ee}^{+,g} \gg |T_{ee}^{-,g}| \sim 0$ and $k_{ee}^{+,g} \simeq 9$.
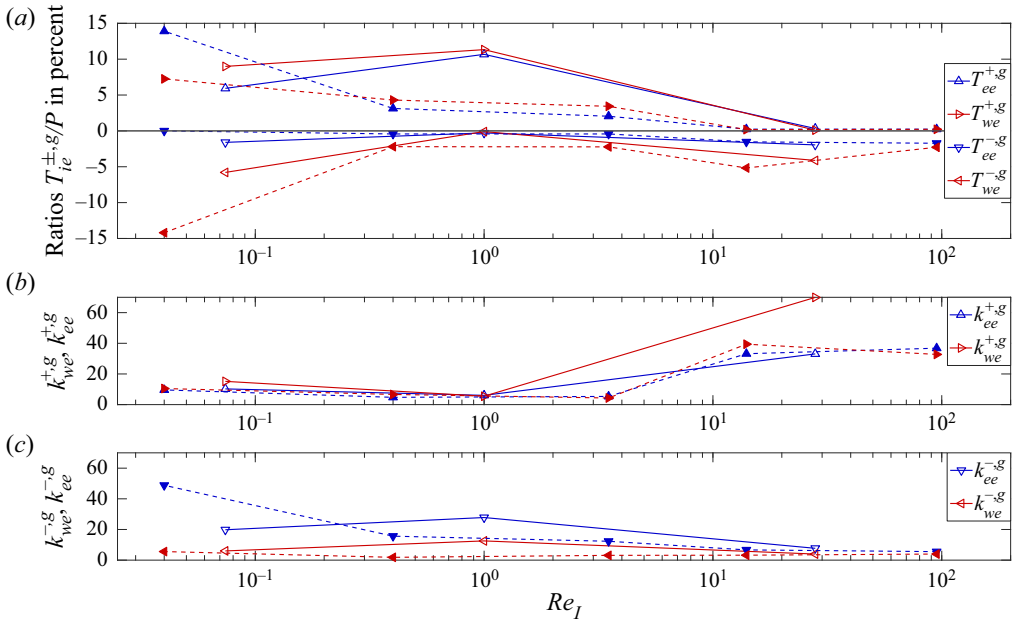
**971** A10-23

Figure 9. Evolution of the detailed transfer from eddies to the GM against $Re_I$. Transfer amplitude divided by forcing $P$ is in (*a*), the average positive scale of transfer is in (*b*) and the average negative scale of transfer is in (*c*). Numerical simulations with $512^3$ points are shown with open symbols and solid lines, and numerical simulations with $256^3$ points are shown with filled symbols and dotted lines.

For high $Re_I$, the eddies take energy from the GM at large scale ($T_{ee}^{+,g} \sim 0 \ll |T_{ee}^{-,g}|$ and $k_{ee}^{-,g} \simeq 5$).

The wave/eddy interaction, i.e. the transfer of energy from eddies to the GM helped by waves, is more subtle. The results of § 4.3 show that the behaviour of the wave/eddy interaction follows the behaviour of the eddy/eddy interaction. However, a scale analysis, that amounts to studying the inertial Reynolds number dependence, provides additional information. At small $Re_I$, and at $512^3$ resolution, the wave/eddy interaction is a net direct transfer that pumps energy from eddies to the GM, since $T_{we}^{+,g} > |T_{we}^{-,g}| \neq 0$ and $k_{we}^{+,g} \simeq 10 - 15 > k_{we}^{-,g} \simeq 5$. At large $Re_I$, the wave/eddy interaction is a transfer that pumps energy from the GM to eddies at large scale, since $|T_{we}^{-,g}| \gg T_{we}^{+,g} \sim 0$ and $k_{we}^{-,g} \simeq 4$. At moderate $Re_I \sim 1$, the positive and negative transfers seem to be dependent on resolution, but when the negative transfer is not zero $|T_{we}^{-,g}| \neq 0$, it seems that the interaction occurs at large scale, as indicated by $k_{we}^{+,g} \simeq 5 - 8$ and $k_{we}^{-,g} \simeq 2$.

### 5.4. *Self-interaction of GM*

The previous section shows that energy transfers to the GM occur mainly at large scale with *ww*, *ew*, *we* and *ee* interactions that vary with *Ro*: globally, the transfers to the GM are stronger at low *Ro* than high *Ro*. Furthermore, the self-interaction of the GM also redistributes energy between the scales of the GM. The interaction of the GM with itself is analysed here.

The self-interaction of the GM is associated to the conservative terms $T_{gg}^{+,g}$ and $T_{gg}^{-,g}$ at typical scales $k_{gg}^{+,g}$ and $k_{gg}^{-,g}$. Figure 10(*a*) shows only $T_{gg}^{+,g}$ against $Re_I$ and $T_{gg}^{-,g} = -T_{gg}^{+,g}$.
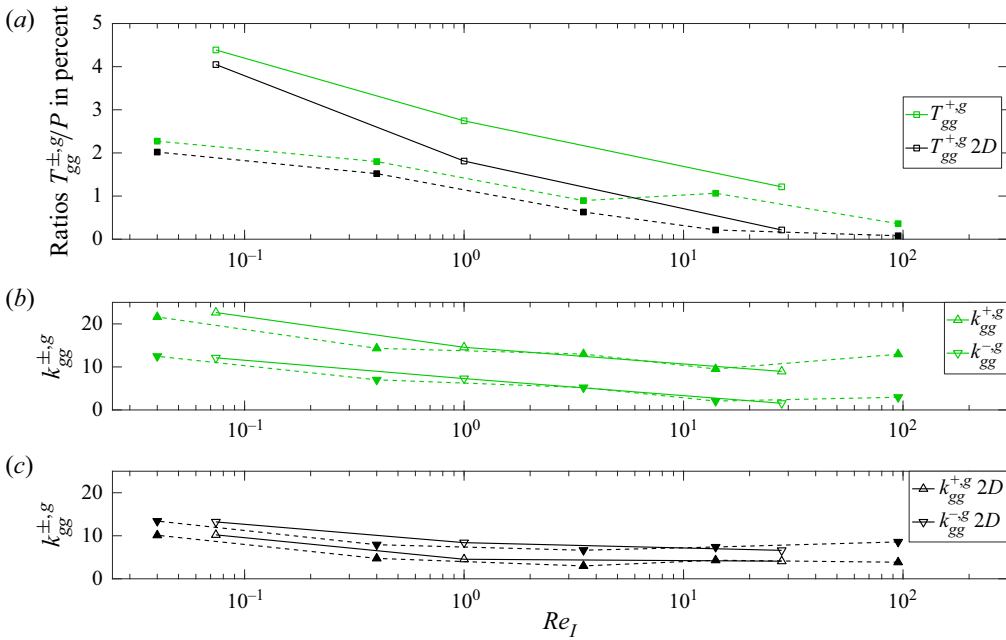
**971** A10-24

Figure 10. Evolution of the detailed cascade of energy involving only the GM against $Re_I$. Transfer amplitude divided by forcing $P$ is in ($a$), the average positive scale of transfer is in ($b$) and the average negative scale of transfer is in ($c$). Numerical simulations with $512^3$ points are shown with open symbols and solid lines, and numerical simulations with $256^3$ points are shown with filled symbols and dotted lines.

We first observe on the figure that the self-interaction amplitude is smaller than that of the wave/wave interaction: $T_{gg}^{+,g}$ decrease from 5 % to 1 % of the total forcing $P$ with $Re_I$, whereas $T_{ww}^{+,g}$ decrease from 25 % to 10 % with $Re_I$. This is consistent with the results of Buzzicotti *et al.* (2018*a*) who also observe that the self-interaction of the 2-D horizontal part of the GM is small compared with other interactions. Our result is also in agreement with the results of Bourouiba *et al.* (2012) who note that the GM energy grows via coupling interactions between the 'fast' and 'slow' modes. Nevertheless, the typical scales are such that $k_{gg}^{+,g} > k_{gg}^{-,g}$ with values decreasing as $Re_I$ increases, and a separation that is roughly constant: $k_{gg}^{+,g} - k_{gg}^{-,g} \simeq 7$–10. This is a signature of a direct cascade for the GM.

However, we considered the GM as a 3-D field. It necessarily includes a vertical component, whose amplitude is larger than its 2-D horizontal component at large $Ro$ (see figure 1*b*). Furthermore, Buzzicotti *et al.* (2018*a*) and Bourouiba *et al.* (2012) have shown that the inverse cascade occurs for the 2-D horizontal velocity of the GM whereas the vertical velocity is considered as a passive scalar with the forward cascade of energy (see Buzzicotti *et al.* 2018*a*). So, we evaluate the self-interaction $T_{gg}^{+,g,2D}$ with typical scale $k_{gg}^{+,g,2D}$ and $k_{gg}^{-,g,2D}$ from the two horizontal components of velocity of the GM. The results are plotted in figure 10(*a,c*), showing that $k_{gg}^{+,g,2D} < k_{gg}^{-,g,2D}$ with a difference between the two roughly constant: $k_{gg}^{-,g,2D} - k_{gg}^{+,g,2D} \simeq 3 - 4$. This means an inverse cascade occurs for the 2-D horizontal part of the GM.

Globally, the self-interaction of the GM increases when $Ro$ decreases for both the 2-D horizontal and vertical components.

## 6. Conclusion

We have proposed a technique to separate IWs from eddies and the GM in rotating turbulence. This computationally and memory intensive separation method has been applied to results of DNS with large-scale forcing, for regimes dominated by rotation ($Ro \ll 1$) ranging from VARFs ($Re_I \ll 1$) to strongly rotating flows ($Re_I \gg 1$). The energy balance equations for IWs, eddies and the GM are established, and their different net transfer terms are computed from the DNS. The forcing mainly feeds the wave part of the flow, but, surprisingly, the injected energy is redistributed to also feed the eddy and GM parts via net transfer terms and conservative terms. We obtain a global picture of the complex set of all net transfers via Sankey diagrams. It appears that eddies are fed by wave/wave, eddy/wave and GM/wave interactions depending on $Ro$ or $Re_I$. Moreover, in rotating turbulence, the GM is supplied by a wave/wave interaction at large scale. This is in agreement with results of the literature for a rotating fluid (Brunet *et al.* 2020; Le Reun *et al.* 2020). However, the eddy/wave interaction appears to also feed the GM at large scale. Other transfers involving the GM can be important such as the wave/eddy interaction or eddy/eddy interaction (both occurring at large scale) that can take energy from the GM depending on the values of $Ro$ and $Re_I$. These interactions are referred to as fast/fast interactions in the literature (Bourouiba *et al.* 2012; Buzzicotti *et al.* 2018*a*), but in the present work we were able to provide a more specific analysis according to wave and eddy parts.

These net transfers do not fully account for the scale dependence of the GM and the rearrangement due to the different types of cascade. We therefore construct a scale-dependent GM evolution equation by including these net transfers and a conservative term. We find that this net transfer term tends to interact at large scale with the GM by providing or taking energy. The conservative term associated to a self-interaction of the GM is weaker than the other terms, showing a direct cascade for the 3-D GM but a reverse cascade for the 2-D GM that feeds the large scales, in agreement with the available literature. Globally, the net transfers and self-interaction are stronger at low $Ro$ than high $Ro$.

The present study provides a rather detailed understanding of the fluxes and energy transfers occurring in rotating flows, but further analyses may still be proposed. First, our forcing is mostly done on the wave part and at large scale, resulting in a split cascade. A more balanced forcing between wave and eddy parts, at different scales, would permit to better understand the transfers between them. Secondly, as often with numerical simulation of turbulence, this separation technique ought to be applied to data at a larger inertial Reynolds number $Re_I$ and lower Rossby number $Ro$, thus requiring higher resolution and an even stronger computational effort. This would permit us to reach a regime of different cascades and interactions closer to the one that appears in actual geophysical and industrial flows. Thirdly, we focused on the supply process that powers the GM. This should be extended to waves and eddies. In particular, the wave/wave, eddy/eddy, eddy/wave, wave/eddy interactions are solely described in terms of scale from the GM point of view, but what are the scales of these interactions from the wave and eddy point of view? Finally, the presented net transfer and conservative terms are quantities averaged over several kinds of triadic interactions, so there is probably room for an analysis of finer-grained mechanisms. Through the study of the structure of nonlinearities, we have identified the wave/wave interaction that we have associated with triadic instability mechanisms as the most studied in the literature, notably because of the importance of the GM. In order to establish an unequivocal link, an in-depth study should be carried out to derive an extension of the formalism introduced in Waleffe (1993) to triadic

interactions involving three fields (wave, eddy and GM), in the same spirit as that carried out in magnetohydrodynamics by Linkmann *et al.* (2016). Furthermore, the physics of these interactions has not been detailed here. It can be understood on a case-by-case basis, either by studying model flows or from physical processes already known. For example, by adding the vorticity equation (2.1), it is possible to understand how eddies are stretched, by the large scale (GM) or by waves. By using the Q criterion (Hunt, Wray & Moin 1988), it is also possible to interpret the interactions in terms of strain-dominated regions or vorticity-dominated regions. On the other hand, the local or non-local nature of the interactions, which has not been explored here, could be studied in order to better understand the typical scales that come into play in the interactions, as in Eyink & Aluie (2009). More generally, it would be necessary to enhance the comprehension of these interaction mechanisms (eddy/eddy, eddy/wave...) whose importance has been shown in this paper.

**Author ORCIDs.**

ⓘ H. Lam https://orcid.org/0000-0002-2604-2714;

ⓘ F.S. Godeferd https://orcid.org/0000-0002-8898-5451.

## Appendix A

In this appendix, inspired by the demonstration of Verma (2019), we detail the analytical proof for $T_{ij}^l = -T_{il}^j$ with $T_{ij}^l = -\langle \widehat{\boldsymbol{\omega}^i \times \boldsymbol{u}^j}, \hat{\boldsymbol{u}}^l \rangle$. The Fourier transform of the nonlinear term can be rewritten as

$$
\begin{aligned}
\widehat{\boldsymbol{\omega}^i \times \boldsymbol{u}^j}(\boldsymbol{k}) &= \sum_{\boldsymbol{p}} \sum_{\boldsymbol{k}=\boldsymbol{p}+\boldsymbol{q}} \hat{\boldsymbol{\omega}}^i(\boldsymbol{q}) \times \hat{\boldsymbol{u}}^j(\boldsymbol{p}) \\
&= \sum_{\boldsymbol{p}} \sum_{\boldsymbol{k}-\boldsymbol{p}-\boldsymbol{q}=0} \hat{\boldsymbol{\omega}}^i(\boldsymbol{q}) \times \hat{\boldsymbol{u}}^j(\boldsymbol{p}) \\
&= \sum_{\boldsymbol{p}} \sum_{\boldsymbol{k}-\boldsymbol{p}-\boldsymbol{q}=0} \overline{\hat{\boldsymbol{\omega}}^i(-\boldsymbol{q})} \times \overline{\hat{\boldsymbol{u}}^j(-\boldsymbol{p})} \text{ by using hermitian symmetry} \\
&= \sum_{-\boldsymbol{P}} \sum_{\boldsymbol{k}+\boldsymbol{P}+\boldsymbol{Q}=0} \overline{\hat{\boldsymbol{\omega}}^i(\boldsymbol{Q})} \times \overline{\hat{\boldsymbol{u}}^j(\boldsymbol{P})} \text{ with } \boldsymbol{P} = -\boldsymbol{p}, \boldsymbol{Q} = -\boldsymbol{q} \\
&= \sum_{\boldsymbol{P}} \sum_{\boldsymbol{k}+\boldsymbol{P}+\boldsymbol{Q}=0} \overline{\hat{\boldsymbol{\omega}}^i(\boldsymbol{Q})} \times \overline{\hat{\boldsymbol{u}}^j(\boldsymbol{P})} \text{ with } \boldsymbol{P} \text{ independent of } \boldsymbol{k} \\
&= \sum_{\boldsymbol{p}} \sum_{\boldsymbol{k}+\boldsymbol{p}+\boldsymbol{q}=0} \overline{\hat{\boldsymbol{\omega}}^i(\boldsymbol{q})} \times \overline{\hat{\boldsymbol{u}}^j(\boldsymbol{p})} \text{ by dropping the upper case,} \quad \text{(A1)}
\end{aligned}
$$

where $\overline{\phantom{x}}$ is the complex conjugate.

By applying the identity $(A \times B) \times C = (C \cdot A)B - (C \cdot B)A$ then

$$\widehat{\omega^i}(q) \times \widehat{u^j}(p) = (\mathrm{i}q \times \widehat{u^i}(q)) \times \widehat{u^j}(p) \tag{A2}$$

$$= (\widehat{u^j}(p) \cdot \mathrm{i}q)\widehat{u^i}(q) - (\widehat{u^j}(p) \cdot \widehat{u^i}(q))\mathrm{i}q \tag{A3}$$

$$\widehat{\omega^i}(q) \times \widehat{u^l}(k) = (\widehat{u^l}(k) \cdot \mathrm{i}q)\widehat{u^i}(q) - (\widehat{u^l}(k) \cdot \widehat{u^i}(q))\mathrm{i}q, \tag{A4}$$

which means that

$$S^{ijl}(k|p|q) = (\widehat{\omega^i}(q) \times \widehat{u^j}(p)) \cdot \widehat{u^l}(k) \tag{A5}$$

$$= (\widehat{u^j}(p) \cdot \mathrm{i}q)(\widehat{u^i}(q) \cdot \widehat{u^l}(k)) - (\widehat{u^j}(p) \cdot \widehat{u^i}(q))(\mathrm{i}q \cdot \widehat{u^l}(k)) \tag{A6}$$

$$S^{ilj}(p|k|q) = (\widehat{\omega^i}(q) \times \widehat{u^l}(k)) \cdot \widehat{u^j}(p) \tag{A7}$$

$$= (\widehat{u^l}(k) \cdot \mathrm{i}q)(\widehat{u^i}(q).\widehat{u^j}(p)) - (\widehat{u^l}(k) \cdot \widehat{u^i}(q))(\mathrm{i}q.\widehat{u^j}(p)) \tag{A8}$$

$$\Rightarrow S^{ijl}(k|p|q) = -S^{ilj}(p|k|q). \tag{A9}$$

With (A9) and (A1) we obtain

$$\sum_k \widehat{\omega^i \times u^j}(k) \cdot \overline{\hat{u}^l(k)} = \sum_k \sum_p \sum_{k+p+q=0} \overline{\hat{\omega}^i(q) \times \hat{u}^j(p) \cdot \hat{u}^l(k)}$$

$$= \sum_k \sum_p \sum_{k+p+q=0} \overline{S^{ijl}(k|p|q)}$$

$$= \sum_k \sum_p \sum_{k+p+q=0} -\overline{S^{ilj}(p|k|q)} \text{ using (A9)}$$

$$= -\sum_k \sum_p \sum_{k+p+q=0} \overline{\hat{\omega}^i(q) \times \hat{u}^l(k) \cdot \hat{u}^j(p)}$$

$$= -\sum_p \sum_k \sum_{k+p+q=0} \overline{\hat{\omega}^i(q) \times \hat{u}^l(k) \cdot \hat{u}^j(p)} \text{ since } k, p \text{ independent}$$

$$= -\sum_k \sum_p \sum_{k+p+q=0} \overline{\hat{\omega}^i(q) \times \hat{u}^l(p) \cdot \hat{u}^j(k)} \text{ by changing name } k \leftrightarrow p$$

$$= -\sum_k \widehat{\omega^i \times u^l}(k) \cdot \overline{\hat{u}^j(k)}.$$

Using this equality and the definition for $\langle \, \rangle$ and $[ \, ]$ given in § 2.2, we finally show that

$$T_{ij}^l = -\langle \widehat{\boldsymbol{\omega}^i \times \boldsymbol{u}^j}, \hat{\boldsymbol{u}}^l \rangle = \sum_{\boldsymbol{k}} Re[\widehat{\boldsymbol{\omega}^i \times \boldsymbol{u}^j}(\boldsymbol{k}, t), \hat{\boldsymbol{u}}^l(\boldsymbol{k}, t)]$$

$$= \sum_{\boldsymbol{k}} Re \left( \frac{1}{T} \int_T \widehat{\boldsymbol{\omega}^i \times \boldsymbol{u}^j}(\boldsymbol{k}) \cdot \overline{\hat{\boldsymbol{u}}^l(\boldsymbol{k})} \, dt \right)$$

$$= Re \left( \frac{1}{T} \int_T \sum_{\boldsymbol{k}} \widehat{\boldsymbol{\omega}^i \times \boldsymbol{u}^j}(\boldsymbol{k}) \cdot \overline{\hat{\boldsymbol{u}}^l(\boldsymbol{k})} \, dt \right)$$

$$= Re \left( \frac{1}{T} \int_T - \sum_{\boldsymbol{k}} \widehat{\boldsymbol{\omega}^i \times \boldsymbol{u}^l}(\boldsymbol{k}) \cdot \overline{\hat{\boldsymbol{u}}^j(\boldsymbol{k})} \, dt \right)$$

$$= - \sum_{\boldsymbol{k}} Re[\widehat{\boldsymbol{\omega}^i \times \boldsymbol{u}^l}(\boldsymbol{k}, t), \hat{\boldsymbol{u}}^j(\boldsymbol{k}, t)] = -T_{il}^j.$$

Since $T_{ij}^l = -T_{il}^j$ then $T_{ij}^j = 0$.

## REFERENCES

BELLET, F., GODEFERD, F.S., SCOTT, J.F. & CAMBON, C. 2006 Wave turbulence in rapidly rotating flows. *J. Fluid Mech.* **562**, 83–121.

BILLANT, P. 2021 Is the Taylor–Proudman theorem exact in unbounded domains? Case study of the three-dimensional stability of a vortex pair in a rapidly rotating fluid. *J. Fluid Mech.* **920**, R1.

BOFFETTA, G., ECKE, R.E. 2012 Two-dimensional turbulence. *Annu. Rev. Fluid Mech.* **44** (1), 427–451.

BOUROUIBA, L., STRAUB, D.N. & WAITE, M.L. 2012 Non-local energy transfers in rotating turbulence at intermediate Rossby number. *J. Fluid Mech.* **690**, 129–147.

BOURY, S., SIBGATULLIN, I., ERMANYUK, E., SHMAKOVA, N., ODIER, P., JOUBAUD, S., MAAS, L.R.M. & DAUXOIS, T. 2021 Vortex cluster arising from an axisymmetric inertial wave attractor. *J. Fluid Mech.* **926**, A12.

BRETHOUWER, G., BILLANT, P., LINDBORG, E. & CHOMAZ, J.-M. 2007 Scaling analysis and simulation of strongly stratified turbulent flows. *J. Fluid Mech.* **585**, 343–368.

BRUNET, M., GALLET, B. & CORTET, P.-P. 2020 Shortcut to geostrophy in wave-driven rotating turbulence: the quartetic instability. *Phys. Rev. Lett.* **124**, 124501.

BUZZICOTTI, M., ALUIE, H., BIFERALE, L. & LINKMANN, M. 2018*a* Energy transfer in turbulence under rotation. *Phys. Rev. Fluids* **3** (3), 034802.

BUZZICOTTI, M., DI LEONI, P.C. & BIFERALE, L. 2018*b* On the inverse energy transfer in rotating turbulence. *Eur. Phys. J.* E **41**, 131.

CAMBON, C., MANSOUR, N.N. & GODEFERD, F.S. 1997 Energy transfer in rotating turbulence. *J. Fluid Mech.* **337**, 303–332.

CAMPAGNE, A., GALLET, B., MOISY, F. & CORTET, P. 2015 Disentangling inertial waves from eddy turbulence in a forced rotating-turbulence experiment. *Phys. Rev.* E **91** (4), 043016.

CARRIERE, P. & MONKEWITZ, P.A. 1999 Convective versus absolute instability in mixed Rayleigh–Bénard–Poiseuille convection. *J. Fluid Mech.* **384**, 243–262.

DAVIDSON, P.A., STAPLEHURST, P.J. & DALZIEL, S.B. 2006 On the evolution of eddies in a rapidly rotating system. *J. Fluid Mech.* **557**, 135–144.

DI LEONI, P.C., COBELLI, P.J. & MININNI, P.D. 2015 The spatio-temporal spectrum of turbulent flows. *Eur. Phys. J.* E **38** (12), 136.

EYINK, G.L. & ALUIE, H. 2009 Localness of energy cascade in hydrodynamic turbulence. I. Smooth coarse graining. *Phys. Fluids* **21** (11), 115107.

GODEFERD, F.S. & MOISY, F. 2015 Structure and dynamics of rotating turbulence: a review of recent experimental and numerical results. *Appl. Mech. Rev.* **67** (3), 030802.

GREENSPAN, H.P. 1968 *The Theory of Rotating Fluids*. Cambridge University Press.

GREENSPAN, H.P. 1969 On the non-linear interaction of inertial modes. *J. Fluid Mech.* **36** (2), 257–264.

HERRING, J.R. 1974 Approach of axisymmetric turbulence to isotropy. *Phys. Fluids* **17** (5), 859–872.

HUERRE, P. & MONKEWITZ, P.A. 1990 Local and global instabilities in spatially developing flows. *Annu. Rev. Fluid Mech.* **22** (1), 473–537.

HUNT, J.C.R., WRAY, A.A. & MOIN, P. 1988 Eddies, streams, and convergence zones in turbulent flows. In *Center for Turbulence Research. Proceedings of the Summer Program 1988*. Center for Turbulence Research.

KAFIABAD, H.A., SAVVA, M.A.C. & VANNESTE, J. 2019 Diffusion of inertia-gravity waves by geostrophic turbulence. *J. Fluid Mech.* **869**, R7.

VAN KAN, A. & ALEXAKIS, A. 2020 Critical transition in fast-rotating turbulence within highly elongated domains. *J. Fluid Mech.* **899**, A33.

LAM, H. 2021 Separation of eddy turbulence and wave turbulence in rotating or stratified flows. PhD thesis, University of Lyon.

LAM, H., DELACHE, A. & GODEFERD, F.S. 2020 Partitioning waves and eddies in stably stratified turbulence. *Atmosphere* **11** (4), 420.

LAM, H., DELACHE, A. & GODEFERD, F.S. 2021 Energy balance and mixing between waves and eddies in stably stratified turbulence. *J. Fluid Mech.* **923**, A31.

LE BARS, M. 2016 Flows driven by libration, precession, and tides in planetary cores. *Phys. Rev. Fluids* **1**, 060505.

LE REUN, T., FAVIER, B., BARKER, A.J. & LE BARS, M. 2017 Inertial wave turbulence driven by elliptical instability. *Phys. Rev. Let.* **119** (3), 034502.

LE REUN, T., FAVIER, B. & LE BARS, M. 2019 Experimental study of the nonlinear saturation of the elliptical instability: inertial wave turbulence versus geostrophic turbulence. *J. Fluid Mech.* **879**, 296–326.

LE REUN, T., FAVIER, B. & LE BARS, M. 2021 Evidence of the Zakharov-Kolmogorov spectrum in numerical simulations of inertial wave turbulence. *Europhys. Lett.* **132** (6), 64002.

LE REUN, T., GALLET, B., FAVIER, B. & LE BARS, M. 2020 Near-resonant instability of geostrophic modes: beyond Greenspan's theorem. *J. Fluid Mech.* **900**, R2.

LINKMANN, M., BERERA, A., MCKAY, M. & JÄGER, J. 2016 Helical mode interactions and spectral transfer processes in magnetohydrodynamic turbulence. *J. Fluid Mech.* **791**, 61–96.

MAFFIOLI, A. 2017 Vertical spectra of stratified turbulence at large horizontal scales. *Phys. Rev. Fluids* **2**, 104802.

MAFFIOLI, A., BRETHOUWER, G. & LINDBORG, E. 2016 Mixing efficiency in stratified turbulence. *J. Fluid Mech.* **794**, R3.

MAFFIOLI, A., DELACHE, A. & GODEFERD, F.S. 2020 Signature and energetics of internal gravity waves in stratified turbulence. *Phys. Rev. Fluids* **5**, 114802.

MARINO, R., MININNI, P.D., ROSENBERG, D. & POUQUET, A. 2013 Emergence of helicity in rotating stratified turbulence. *Phys. Rev. E* **87**, 033016.

MININNI, P.D., ALEXAKIS, A. & POUQUET, A. 2009 Scale interactions and scaling laws in rotating flows at moderate Rossby numbers and large Reynolds numbers. *Phys. Fluids* **21** (1), 015108.

MONKEWITZ, P.A., HUERRE, P. & CHOMAZ, J.-M. 1993 Global linear stability analysis of weakly non-parallel shear flows. *J. Fluid Mech.* **251**, 1–20.

MONSALVE, E., BRUNET, M., GALLET, B. & CORTET, P.-P. 2020 Quantitative experimental observation of weak inertial-wave turbulence. *Phys. Rev. Lett.* **125** (25), 254502.

MORY, M. & HOPFINGER, E.J. 1985 Rotating turbulence evolving freely from an initial quasi 2D state. In *Macroscopic Modelling of Turbulent Flows* (ed. U. Frisch, J.B. Keller, G.C. Papanicolaou & O. Pironneau), pp. 218–236. Springer.

MOULIN, F. & FLÓR, J.-B. 2006 Vortex–wave interaction in a rotating stratified fluid: WKB simulations. *J. Fluid Mech.* **563**, 199–222.

MOULIN, F.Y. & FLÓR, J.-B. 2005 Experimental study on wave breaking and mixing properties in the periphery of an intense vortex. *Dyn. Atmos. Oceans* **40** (1–2), 115–130.

NEWELL, A.C. 1969 Rossby wave packet interactions. *J. Fluid Mech.* **35** (2), 255–271.

RILEY, J.J., METCALFE, R.W. & WEISSMAN, M.A. 1981 Direct numerical simulations of homogeneous turbulence in density-stratified fluids. *AIP Conf. Proc.* **76** (1), 79–112.

SAGAUT, P. & CAMBON, C. 2018 *Homogeneous Turbulence Dynamics*, 2nd edn. Springer.

SAVVA, M.A.C., KAFIABAD, H.A. & VANNESTE, J. 2021 Inertia-gravity-wave scattering by three-dimensional geostrophic turbulence. *J. Fluid Mech.* **916**, A6.

SESHASAYANAN, K. & ALEXAKIS, A. 2018 Condensates in rotating turbulent flows. *J. Fluid Mech.* **841**, 434–462.

SHARMA, M.K., VERMA, M.K. & SAGAR, C. 2019 Anisotropic energy transfers in rapidly rotating turbulence. *Phys. Fluids* **31** (8), 085117.

SMITH, L.M. & WALEFFE, F. 1999 Transfer of energy to two-dimensional large scales in forced, rotating three-dimensional turbulence. *Phys. Fluids* **11** (6), 1608–1622.

STAPLEHURST, P.J., DAVIDSON, P.A. & DALZIEL, S.B. 2008 Structure formation in homogeneous freely decaying rotating turbulence. *J. Fluid Mech.* **598**, 81–105.

VERMA, M.K. 2019 *Energy Transfers in Fluid Flows: Multiscale and Spectral Perspectives*. Cambridge University Press.

WALEFFE, F. 1993 Inertial transfers in the helical decomposition. *Phys. Fluids* A*: Fluid Dyn.* **5** (3), 677–685.

YAROM, E. & SHARON, E. 2014 Experimental observation of steady inertial wave turbulence in deep rotating flows. *Nature Phys.* **10** (7), 510–514.

ZEMAN, O. 1994 A note on the spectra and decay of rotating homogeneous turbulence. *Phys. Fluids* **6** (10), 3221–3223.